

UNIVERSITÀ POLITECNICA DELLE MARCHE
Repository ISTITUZIONALE

The effect of initial microstructure on the creep response of austenitic stainless steels: the case of annealed and friction stir welded AISI 316L tested between 550 and 650 °C

This is the peer reviewd version of the followng article:

Original
The effect of initial microstructure on the creep response of austenitic stainless steels: the case of annealed and friction stir welded AISI 316L tested between 550 and 650 °C / Spigarelli, S., Cabibbo, M., Ciccarelli, D., Santoni, A., Regev, M.. - In: JOURNAL OF MATERIALS SCIENCE. - ISSN 0022-2461. - 60:39(2025), pp. 18177-18200. [10.1007/s10853-025-10935-1]

Availability:
This version is available at: 11566/365893 since: 2026-11-02T10:29:05Z

Publisher:

Published
DOI:10.1007/s10853-025-10935-1

Terms of use:

The terms and conditions for the reuse of this version of the manuscript are specified in the publishing policy. The use of copyrighted works requires the consent of the rights' holder (author or publisher). Works made available under a Creative Commons license or a Publisher's custom-made license can be used according to the terms and conditions contained therein. See editor's website for further information and terms and conditions.
This item was downloaded from IRIS Università Politecnica delle Marche (https://iris.univpm.it). When citing, please refer to the published version.

Publisher copyright:

Springer (article) - Postprint/Author's accepted Manuscript

This version of the article has been accepted for publication, after peer review (when applicable) and is subject to Springer Nature's AM terms of use https://www.springernature.com/gp/open-research/policies/accepted-manuscript-terms, but is not the Version of Record and does not reflect post-acceptance improvements, or any corrections. The Version of Record is available online at: 10.1007/s10853-025-10935-1.

(Article begins on next page)

29 November 2026

Spigarelli, S., Cabibbo, M., Ciccarelli, D. *et al.* The effect of initial microstructure on the creep response of austenitic stainless steels: the case of annealed and friction stir welded AISI 316L tested between 550 and 650 °C. *J Mater Sci* 60, 18177–18200 (2025). https://doi.org/10.1007/s10853-025-10935-1

- **Received25 February 2025**
- **Accepted21 April 2025**
- **Published22 May 2025**
- **Version of record22 May 2025**
- **Issue dateOctober 2025**
- **DOIhttps://doi.org/10.1007/s10853-025-10935-1**

Accepted draft

https://link.springer.com/article/10.1007/s10853-025-10935-1

https://doi.org/10.1007/s10853-025-10935

The effect of initial microstructure on the creep response of austenitic stainless steels: the case of annealed and Friction Stir Welded AISI 316L tested between 550 and 650°C

S.Spigarelli[1], M.Cabibbo[1], D.Ciccarelli, A.Santoni[1], M.Regev[2]

1. DIISM, Università Politecnica delle Marche, 60131, via Brecce Bianche 60131 Ancona, Italy;
2. Department of Mechanical Engineering, Braude College, P.O. Box 78, Karmiel 2161002, Israel

Abstract

The creep behavior of AISI 316L stainless steel in the 1/8 hard initial condition was examined following Friction Stir Welding (FSW) at temperatures ranging from 550°C to 650°C. For comparison, a limited number of tests were also performed on unwelded samples. Microstructural analysis revealed that FSW produced a structure densely populated with finely spaced twins. The hardness of both the initial 1/8 hard and FSWed states was significantly higher than that of the annealed condition. The minimum creep rates observed in the FSWed material were slightly lower than those measured in the annealed state under very high stress conditions. However, under the lowest stress levels used in this study, the FSWed material exhibited minimum creep rates approximately an order of magnitude lower than those of the annealed steel. This behavior was interpreted using a physically-based constitutive model that accurately captured the dependence of the minimum creep rate on applied stress and temperature, as established by literature data for annealed material. The model accounted for the dominant strengthening mechanisms across different regimes: in the high stress/low temperature regime, dislocation motion is impeded by dense dislocation cell walls formed during loading; in the low stress/high temperature regime, dislocation mobility is limited by interactions with precipitates. While the same model provided a qualitative understanding of the creep response of FSWed AISI 316L, the absence of a reliable

physical model to quantify the strengthening effect of twinning during creep precludes accurate predictions of the minimum strain rate without relying on empirical fitting procedures.

Keywords: Creep, austenitic stainless steel, microstructure , friction stir welding

1. Introduction

Friction stir welding (FSW) is a solid-state joining process that has been successfully applied to a wide range of metals [1]. In FSW, friction between the workpiece and a non-consumable rotating tool generates heat, softening the material. As the tool is pressed and rotates against the workpiece, it mechanically deforms and mixes the two parts, creating a solid-state bond.

FSW has already been successfully used to join AISI 316L stainless steel plates. This austenitic stainless steel is widely employed in industrial applications due to its excellent properties, including high strength at elevated temperatures and creep resistance. As expected, also in AISI 316L the microstructure of the FSWed (Friction Stir Welded) zone is significantly influenced by its thermal and deformation history. For instance, Shashi Kumar et al. [2] observed shear bands in the weld zone, where the intensity of these bands was strongly affected by the deformation temperature. Additionally, the tensile strength of the joints varied with the rotational speed of the tool. The local microstructural characteristics are determined by the intense force, deformation, and heat generated in the stir zone under the rotating tool. In turn, they are highly dependent on the process parameters used during welding. Understanding the structure-property relationships and their specific correlation with FSW requires in-depth analysis. For a broader discussion of this subject, reference to specialized literature is recommended [3]. However, one critical property is invariably overlooked when studying FSWed materials: creep response. In the case of AISI 316L, this knowledge gap is particularly relevant due to its inherently high creep resistance.

The fundamental characteristics of creep behavior in wrought austenitic stainless steels have been extensively researched over several decades. Recently, there has been a resurgence of interest in the creep response of AISI 316L steel, particularly due to its increasing application in components produced through additive manufacturing techniques. In this context, a recent study [4] has undertaken a review of existing literature on the subject, with the objective of establishing a coherent framework that elucidates the creep response of both wrought and additively manufactured materials. The primary conclusion of the study, which interested readers can consult for a

comprehensive analysis of the results found in the bibliography, is that the mid- and long-term creep behavior of AISI 316 steel is primarily influenced by the precipitation of intragranular carbides. The precipitation of these particles occurs in AISI 316 and even 316L after durations that are compatible with mid-term creep experiments. The interaction between carbides and carbonitrides, the latter in nitrogen-containing steels, impedes dislocation movement, thereby improving creep strength.

The development of a clearly defined substructure of subgrains, resulting from significant recovery processes, is a characteristic hallmark of creep behavior in class-M alloys. Austenitic stainless steels exhibit low stacking fault energy [5], which results in a significant separation of partial dislocations. This phenomenon markedly diminishes dislocation mobility, leading to restricted recovery. A transition in the substructure has thus been identified, shifting from a subgrain morphology following creep at elevated temperatures and low stress levels to a microstructure characterized by dislocation tangles and cells under high stress conditions. This phenomenon was documented in AISI 316 steel by Kestenbach et al., who conducted tests at temperatures between 600 and 800°C [6, 7]. While some subgrains may form with prolonged exposure to elevated temperatures, even at 550°C, cells defined by dense dislocation walls appear during brief testing periods under high stress at this temperature [8]. The presence of precipitates impedes the rearrangement of dislocations into a subgrain structure, thereby enhancing the stability of a planar dislocation configuration. Thus, under lower stress conditions and extended durations, the permanence of a stable planar arrangement of dislocation tangles, accompanied by a dispersion of precipitates, has been documented at 550°C by Mathew and colleagues.

Although the material response under intermediate and low stresses, along with the pivotal role of precipitation in influencing this response, has been adequately elucidated, the controlling mechanism in the high stress regime -where testing time is insufficient for precipitation to occur - remains an interesting topic which still deserves to be discussed. In this context, the present study aims to clarify several key points, specifically:

i. The quantification of the effect of Friction Stir Welding on the short-term creep response of AISI 316L plates in 1/8 hard initial state.

ii. The interpretation of the creep mechanisms governing behavior in the high stress regime, within a framework applicable to wrought similar steels; this coherent framework should be founded on a set of constitutive equations with solid, albeit simplified, physical underpinnings.

2. Materials and methods

2.1 Material and processing

The study utilized commercially available AISI 316L stainless steel plates in 1/8 hard state, measuring 200 mm x 200 mm and 3 mm in thickness. The chemical composition was C=0.019, Cr=16.7, Ni=10.2, Mo=2.08, Mn=1.34, N=0.066 (wt.%). The plates underwent bead-on-plate friction stir welding on both sides, employing a SHARNOA M32 CNC milling machine. The welding tool was a 100 mm long tungsten carbide (WC) cylinder with a diameter of 16 mm. Optimization of the welding parameters was achieved through various experimental conditions, specifically by adjusting combinations of rotational and transverse speeds. Prior to initiating the welding process, the tool was rotated in place for 15 seconds upon contact with the upper surface of the plate to facilitate heating. The selection criteria for optimal welding parameters focused on the integrity of the tool and visual assessments of the weld quality. Subsequently, four metallographic specimens were extracted from a plate welded under these conditions, with the first specimen taken from the initial quarter of the seam, the second from the second quarter, and so forth, to eliminate the possibility of internal porosity or cracking. Based on these evaluations, the optimal welding parameters were determined to be a rotational speed of 600 rpm and a transverse speed of 100 mm/min.

Dog-bone shaped creep samples were machined from the FSWed plates, with a gauge length of 25 mm oriented perpendicular to the welding direction (Figure 1). This configuration ensured that only

the two extreme ends of the gauge length represented the base material, while the remainder consisted of weld metal.

2.2 Creep experiments

The creep samples were tested by Constant Load Experiments (CLEs) and Variable Load Experiments (VLEs). During the CLEs, the samples were subjected to a constant load, P, until reaching the tertiary region and, in most instances, fracture. In the VLEs, the initial load was incrementally increased once the sample achieved what was believed to be the minimum creep-rate range.

Creep tests were conducted at temperatures of 550, 600, and 650°C (823, 873 and 923 K) . For reference purposes, 6 additional experiments were carried out at 600 and 650°C on as-received (unwelded) samples. All investigated conditions are summarized in Table 1, which details the nominal stress ($\sigma = P/A_0$, where A_0 represents the initial area of the gauge's transverse section) and the corresponding minimum creep rate values. In one instance, the furnace was turned off immediately after loading to measure instantaneous strain.

The testing temperature was measured using four thermocouples, while elongation was continuously monitored with an LVDT (Linear Variable Differential Transformer).

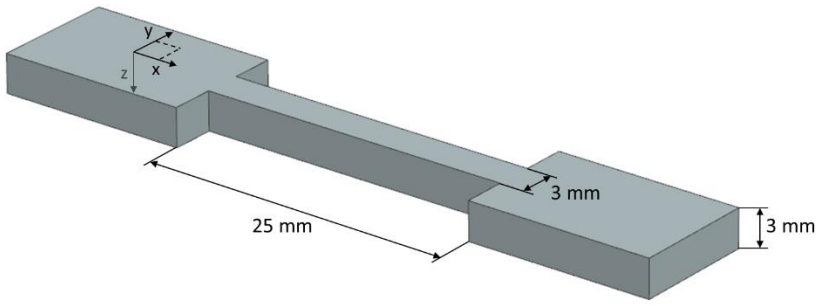


Fig.1 Geometry of the creep sample. For samples machined from friction stir welded (FSWed) plates, the welding direction was oriented parallel to the y-axis, aligning precisely with the center of the gauge length. Consequently, 64% of the gauge length was subjected to the direct influence of the tool on both sides. The Figure also shows the x,y and z directions mentioned in the text

Table 1. Summary of the experimental conditions.

designation	temperature [°C]	Nominal stress [MPa]	Minimum creep rate [s^{-1}]	Overall duration of high temperature exposure* [h]
FSWed AISI 316L plate (1/8 hard)				
VLE1	550	380	$4.1x10^{-8}$	149
		400	$1.4x10^{-7}$	
VLE3	550	250	Not reached	958
		350	$5.3x10^{-9}$	
CLE3	600	250	$7.5x10^{-9}$	22
VLE2	600	300	$7.0x10^{-8}$	119
		330	$8.0x10^{-7}$	
CLE2	600	350	$3.4x10^{-6}$	6
CLE1	600	375	$1.0x10^{-5}$	3
CLE4	650	250	$1.0x10^{-6}$	22
CLE5	650	275	$4.4x10^{-6}$	5
CLE6	650	225	$2.0x10^{-7}$	166
VLE7	650	150	$7.5x10^{-10}$	980
		208	$2.0x10^{-7}$	
AISI 316L plate (1/8 hard)				
CLE9	600	340	$4.6x10^{-6}$	70
VLE5	600	300	$2.3x10^{-7}$	47
		360	$4.0x10^{-6}$	
VLE6	600	250	$6.0x10^{-9}$	48
		320	$1.3x10^{-6}$	
		360	$6.0x10^{-6}$	
CLE7	650	225	$6.3x10^{-7}$	45
CLE8	650	240	$1.0x10^{-7}$	73
VLE4	650	200	$1.5x10^{-7}$	100
		252	$4.5x10^{-6}$	

* includes soaking time, creep test duration and any extra-time the samples remained in the furnace at the testing temperature after rupture (number rounded up to the next highest integer).

2.3 Microstructural characterization

Optical microscopy was conducted on a Leica DMi8 microscope after selected samples underwent standard metallographic preparation, which included grinding, polishing, etching with 15ml HCl+10ml HNO_3+10 ml CH_3COOH. Vickers hardness (*Hv*) was assessed using a QNESS 60+ EVO microhardness tester on polished samples (applied load 300g).

Transmission electron microscopy (TEM) was employed to examine the microstructure of the as-welded and crept specimens. TEM samples were extracted from one untested specimen and two crept specimens (CLE3 and VLE3, see Table 1).

TEM thin foils were mechanically prepared by polishing down to 0.25 μm, followed by punching and dimpling both sides of the TEM discs, and finally thinned to electron transparency using a precise ion polishing device (PIPS, GATANTM) operating at 12 V. The Ar^+ twin beam was configured to progressively decrease incident angles from 8 to 4° relative to the thin foil surface.

All TEM inspections were conducted using a PhilipsTM CM-200® microscope operating at 200 keV, equipped with a double-tilt specimen holder and a liquid nitrogen cooling stage.

3. Results

3.1 Initial microstructure

Figures 2 and 3 present an examination of the microstructure of the friction stir welded plate, as analyzed through optical microscopy. The weld nugget zone, below the oxide superficial layer, formed during tool action, reveals “layered symmetrical structure” which consists of:

I) A thin (150-200 μm) layer of ultrafine grains.

II) A further layer 200-250 μm thick formed by deformed grains.

III) The bulk of the sample, formed by equiaxed fine grains, less than 50 μm in size, interspersed with δ-ferrite streaks and particles.

The bulk of the deformed zone thus underwent extensive dynamic recrystallization and moderate grain growth, resulting in fine equiaxed grains.

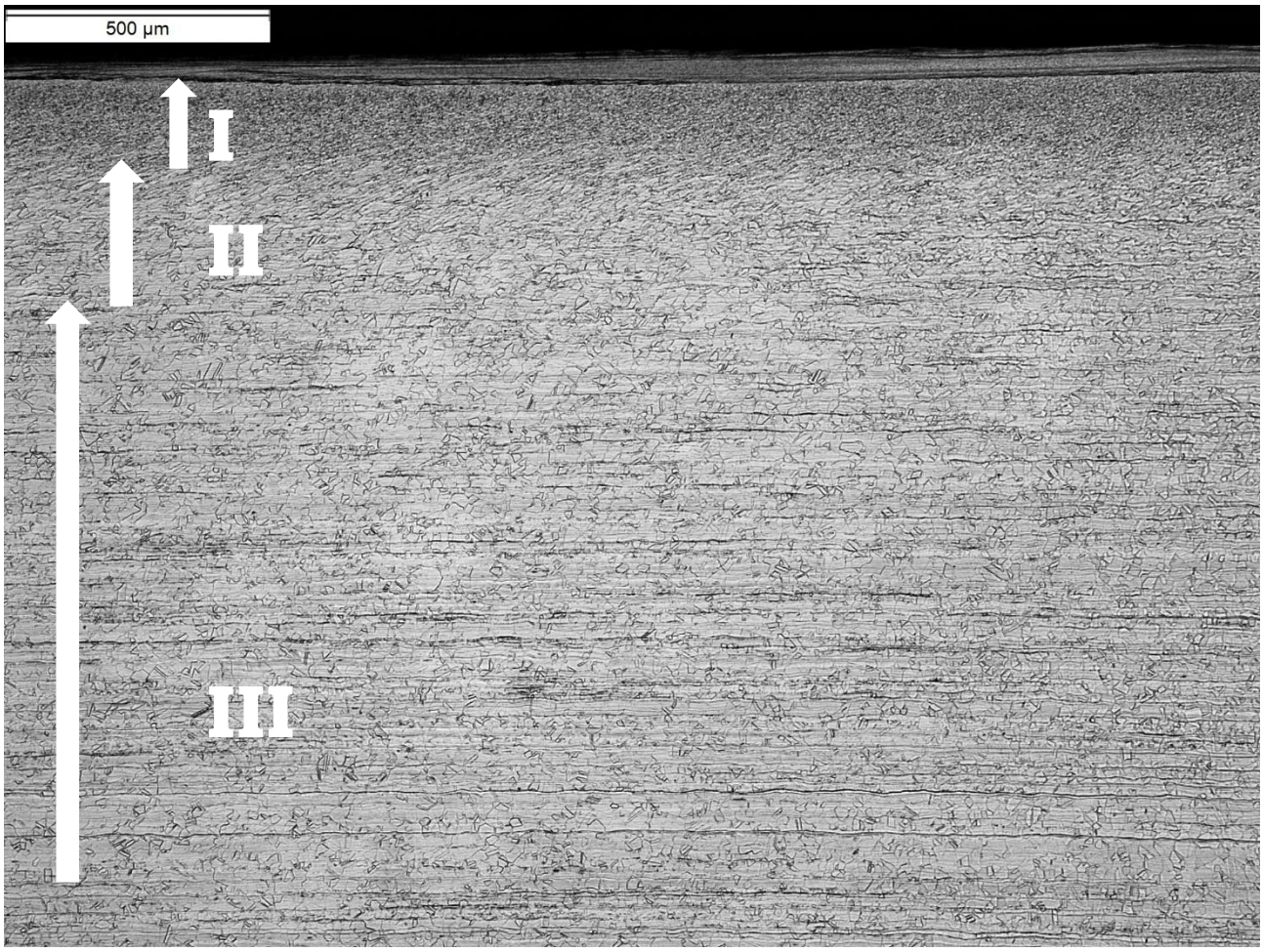
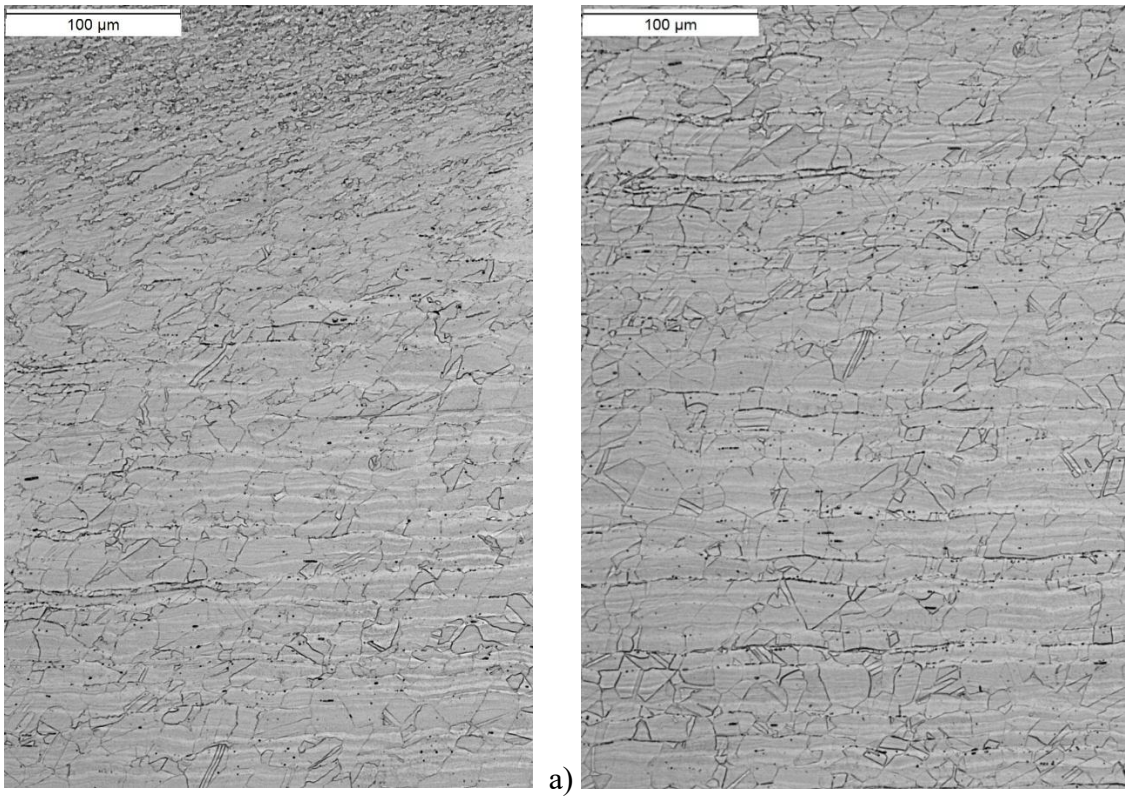


Fig.2 Microstructure in the weld (nugget) at low magnifications; the different layers, described in the text, can be easily recognized. Dark elongated thin bands are formed by δ-ferrite



a) b)

Fig.3 Microstructure in the weld (nugget) at higher magnifications; in a) the ultrafine-grained layer close to the surface can be easily appreciated in the upper part of the micrograph. In b), the fine and homogeneous recrystallized grain size in the bulk of the weld can be observed; fragmented streaks and isolated dark particles are formed by δ-ferrite

Figure 4 illustrates the differences in hardness between an unwelded creep sample and a specimen machined from friction stir welded plates. Micro-hardness was measured along the gauge length (xy plane). Thus, for the FSWed sample, these measurements were conducted perpendicularly to the direction of tool advancement. The average *Hv* values for the as-received plate and the FSWed joint were 191 ± 1 and 231 ± 6 VHN (Vickers Hardness number) respectively. The average hardness value of the unwelded material is 40 VHN greater than the typical values reported for AISI 316L annealed plate, as referenced in [9]. In FSWed samples, the gauge length extremes exhibit a hardness comparable to that of the unwelded metal.

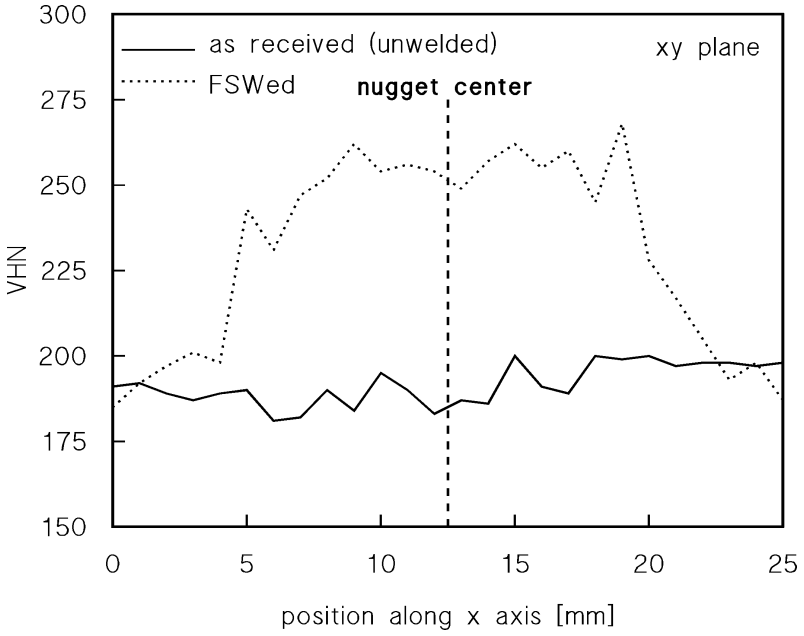


Fig.4 Microhardness in the x direction on the xy surface of the creep sample for unwelded and FSWed materials

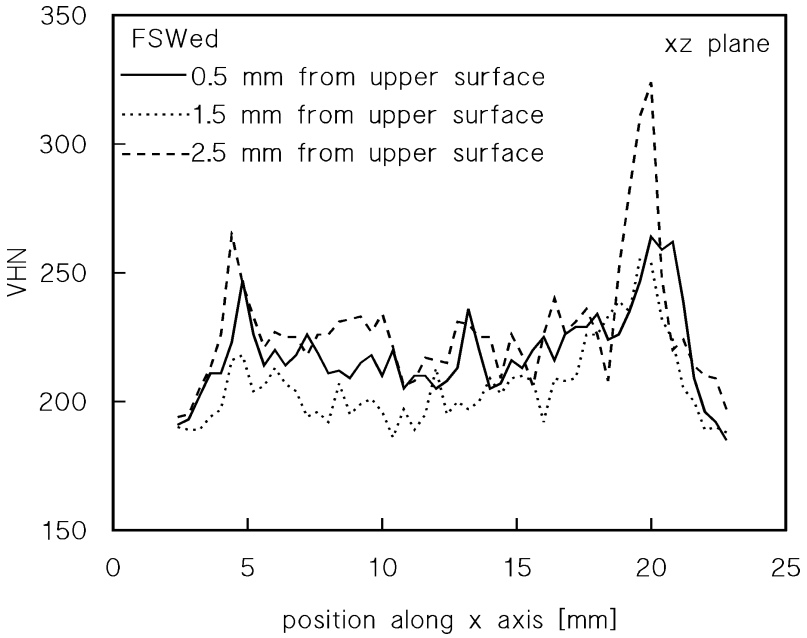


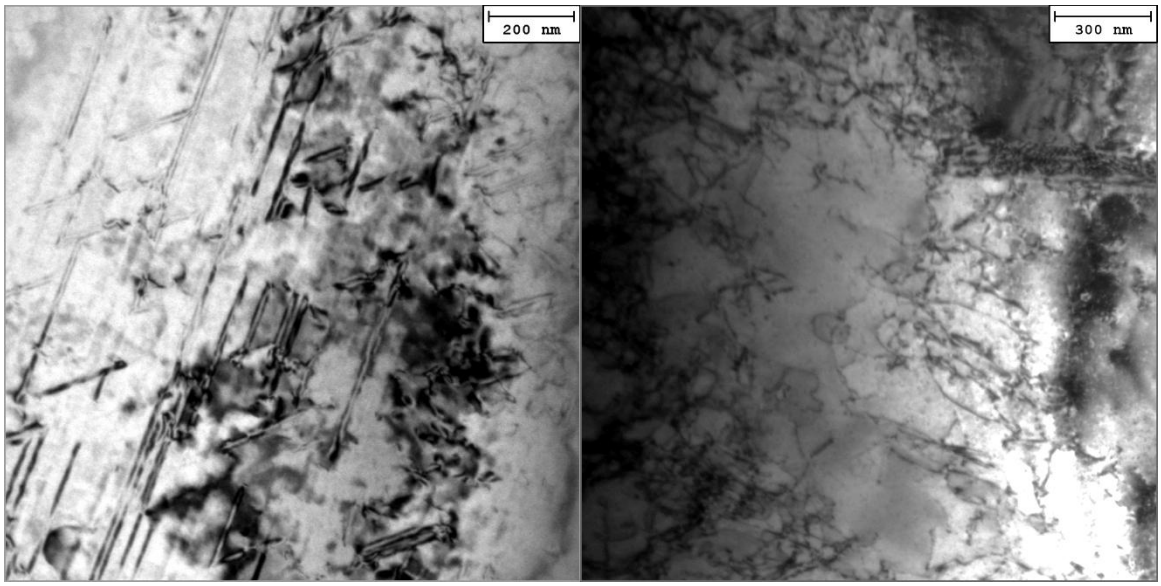
Fig.5 Microhardness in the x direction on the xz surface of the creep sample for FSWed steel. The *Hv* measurements were carried out on 3 parallels straight lines, two at 0.5mm from each (upper and lower) surface, and the last along the center of the gauge length

Figure 5 illustrates the hardness values measured along the gauge length, on the xz plane, of a friction stir welded sample. Hardness measurements were conducted along three linear paths, located at distances of 0.5 mm, 1.5 mm, and 2.5 mm from one of the surfaces (xy plane). The

average *Hv* values, in these cases, were 219 ± 2, 206 ± 12 and 228 ± 3 VHN. The high hardness observed in the central region of the FSW joint has been validated. On the other hand, the disparity in hardness between the stir zone and the base metal is notably diminished in the xz section compared to the surface of the sample (xy plane). The observed phenomenon can be ascribed to the presence of the superficial layers of ultrafine-grains and deformed grains, just below both surfaces of the weld zone. In contrast, the internal microstructure displays the equiaxed, fully recrystallized grains, which closely resemble those homogeneously found in the unwelded plate. However, the hardness in the bulk of the weld is still 15-40 and 55-90 VHN higher than parent metal (1/8 hard plate) and annealed material respectively.

TEM microstructural inspections across the nugget zone of the FSWed uncrept sample revealed the most probable microstructural cause of the particularly high hardness values recorded in this region. Most of the austenite grains in the 316L FSWed nugget exhibit a significant presence of twinning. These twins are predominantly narrow and straight, extending from one grain boundary to the opposite one. In some cases, families of parallel twins intersect with other sets of parallel twins oriented in a different crystallographic direction, typically forming an approximately perpendicular arrangement (Figure 6a). This indicates that a microstructural strengthening mechanism, driven by families of austenite twins, contributes to the mechanical strength of the FSWed nugget zone. Additionally, the austenite grains are decorated with a substantial number of tangled dislocations, which do not form well-organized cell structures (Figure 6b).

Figure 6 shows that, despite being recrystallized, the microstructure of the FSWed plates still contains a significant number of internal defects, including twins and tangled dislocations. This makes it substantially different from the typical annealed state.



a) b)

Fig.6 Representative BF-TEM (Bright Field TEM): a. families of twins running from boundary to boundary of the austenite grain; b. tangled dislocations till not forming cell structures within the grains

3.2 Instantaneous strain after loading

The yielding stress of annealed AISI 316L is marginally above 100 MPa at 550°C and maintains relative stability up to 650°C [10]. As a result, under the stress conditions employed in this study, all samples exhibited considerable plastic strains immediately upon loading. In a conventional creep testing apparatus, such as those utilized in this research, specimens are subjected to a predetermined load, conveyed via a lever arm affixed to a fixed base. As the sample undergoes elongation, the resulting inclination of the lever arm leads to a decrease in the lever gain ratio, which corresponds to a reduction in the applied stress. This discrepancy is rectified by an electric motor that realigns the lever to its appropriate position. The system is adept at measuring deformation at slow strain rates, which are characteristic of creep behavior. When the applied stress significantly surpasses the yielding stress, a marked immediate elongation occurs, resulting in a tilt of the lever and a rapid reduction in the sample's stress. Subsequently, the loading lever is realigned to restore the correct load. This sequence of events may introduce specific inaccuracies in the assessment of

instantaneous plastic strain. The resulting scatter in the engineering strain (e) versus stress (s) is clearly illustrated in Figure 7. Conversely, an accurate estimation of the instantaneous strain during loading is crucial for effectively characterizing the creep response in the high-stress regime. Thus, an equation in the form

$$s = R_y + C' e^{m_e} \quad (1)$$

where R_y is the yield stress at the investigated temperature, C' is a temperature-dependent constant and, for the sake of simplicity, m_e is a temperature-independent parameter, was used to describe the experimental values of the strain as a function of nominal applied stress. The data presented in Figure 7 illustrates the curves obtained with C'= 625, 500, and 450 MPa, corresponding to temperatures of 550, 600, and 650°C, respectively. The strain exponent for the as-received material was determined to be 0.3, while for the FSWed material, it was 0.38. The yield strengths were tentatively estimated at 100 MPa and 150 MPa, respectively.

The curves at 600°C are favorably compared in the figure with the measured value of the instantaneous strain obtained from the test that was interrupted immediately after loading.

A comparative analysis of the curves shown in Figure 7, in conjunction with those cited in [11], reveals that the material in question demonstrates superior strength compared to the 0.052% C annealed AISI 316 steel studied by Morris and Harries. This conclusion is further substantiated by the *Hv* values obtained for both unwelded and friction stir welded samples, which significantly exceed those commonly associated with annealed materials from the AISI 316 family. The data on instantaneous strain in relation to applied stress in [11], can be thus employed to ascertain the temperature dependence of the constant C' in equation (1) for an annealed steel. With a specified value of m_e=0.5, as proposed by Morries and Harries, the values derived for C are 750, 590, and 440 MPa at temperatures of 550, 600, and 650°C, respectively. Utilizing Equation (1) to estimate the instantaneous strain upon loading, the dotted curves depicted in Figure 7 are generated.

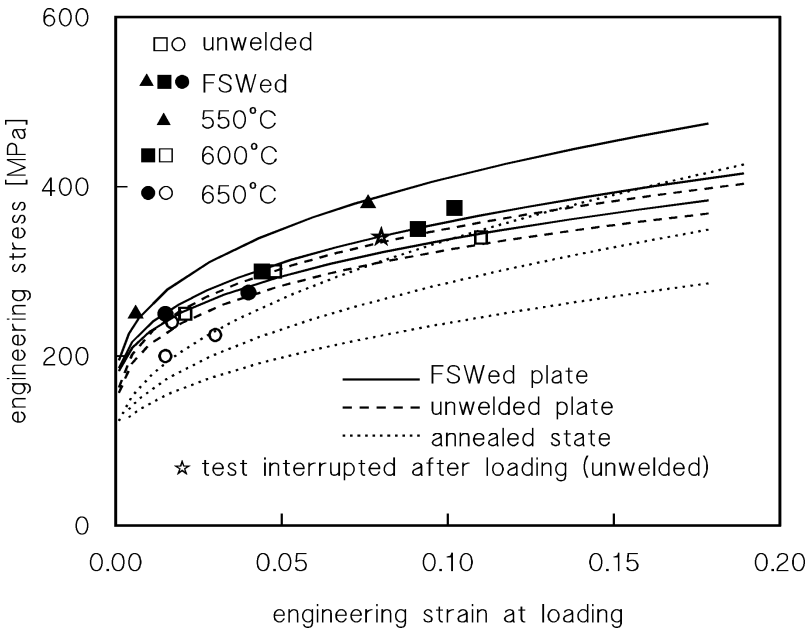


Fig.7 Experimental values of engineering strain immediately after loading. The focus is exclusively on measured strains exceeding 0.5%. The Figure also illustrates the curves derived from Equation (1), based on the assumption that the exponent *C'* is solely dependent on temperature, while the variable m_e is influenced only by the initial state. The solid and dashed lines represent the friction stir-welded and unwelded samples, respectively. Notably, as the temperature decreases from 650°C to 600°C, the difference between the friction stir-welded and unwelded materials gradually lessens. The Figure also shows the 3 curves describing the instantaneous strain at loading for AISI 316 tested in annealed condition (R_y=100 MPa, m_e=0.5, *C'* =750, 590, and 440 MPa at 550, 600, and 650°C, respectively, obtained from data in [11])

While Equation (1) does not seek to deliver a physically accurate depiction of material behavior under the specified conditions, it provides a sufficiently precise quantification of the instantaneous strain during loading for CLEs and the initial phase of VLEs. For subsequent loading increments in VLEs, the estimation of instantaneous elongation was directly obtained from LVDT measurements.

3.3 Creep results

Figure 8 illustrates the characteristics of representative creep curves derived from CLEs and VLEs for FSWed material. Typically, these curves exhibit a brief primary phase, followed by a minimum creep rate range culminating in an extended tertiary stage. The minimum creep rate is observed at lower strains as the applied stress decreases. Similar behavior is noted in the unwelded metal (Figure 9).

Figure 10 depicts the dependence of minimum creep rate on nominal, i.e. initial, applied stress (*s*) for both FSWed and unwelded samples. The figure indicates that at 600°C, the behaviors of the as-received and FSWed samples are quite comparable. Only at the highest temperature, the FSWed steel appears to exhibit slightly lower creep rates.

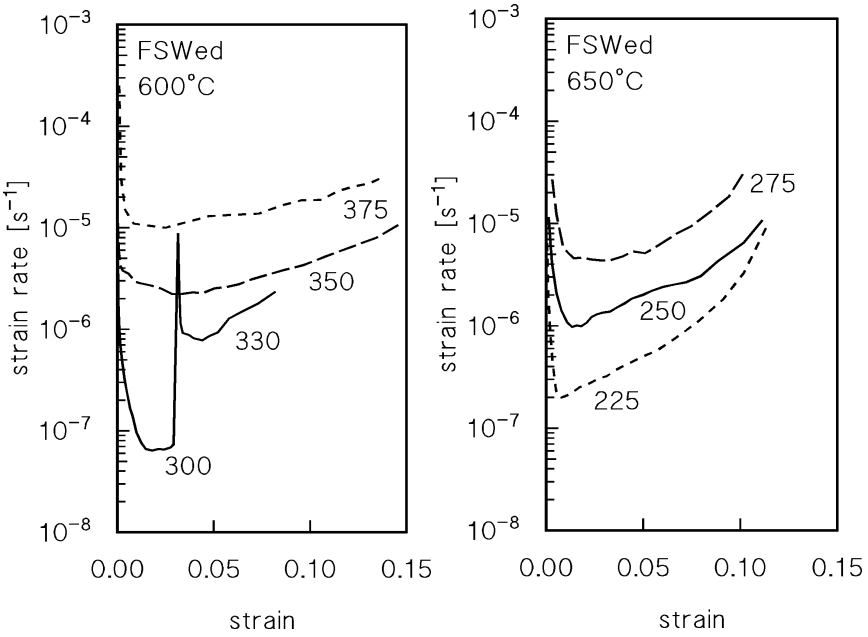


Fig.8 Strain rate *vs* strain representative creep curves for the FSWed steel

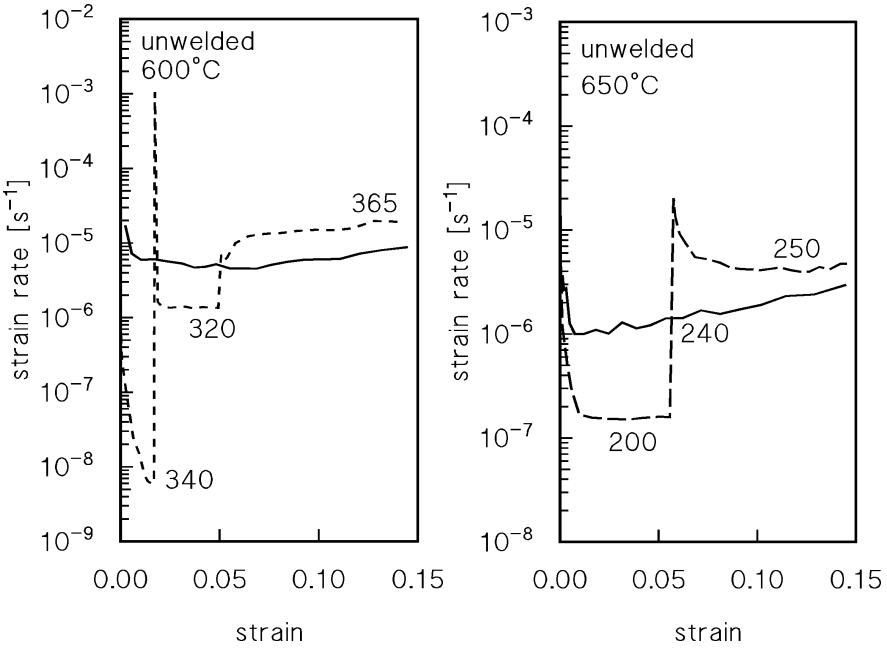


Fig.9 Strain rate *vs* strain representative creep curves for the unwelded steel

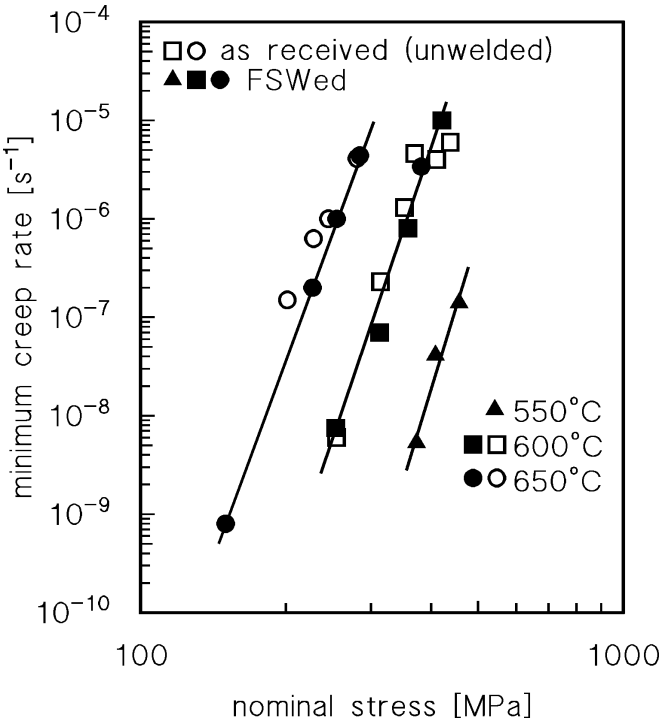


Fig.10 The relationship between the minimum creep rate and nominal stress. The open data points correspond to tests conducted on unwelded steel, while the solid symbols indicate tests performed on FSWed material. Notably, since the CLEs and VLEs align along the same curves, the figure does not differentiate between these two types of tests

The comparison of the creep responses between unwelded and friction stir welded steel is further substantiated by plotting the minimum creep rate as a function of the true applied stress following the loading process $\sigma=s\ (1+e)$, where e is the engineering strain accumulated immediately after each loading operation (Figure 11). The engineering strain following the second or third loading of the VLEs encompasses both the instantaneous strain from previous loading operations and the creep strain accumulated up to that point. The Figure further shows the creep results reported in [12], which offers a comprehensive compilation of minimum creep rate data for three annealed AISI 316 and 316L steels, each characterized by varying concentrations of carbon and nitrogen (0.02, 0.06, and 0.08 wt.% for carbon; 0.08, 0.019, and 0.025% for nitrogen, respectively). Some of the creep data were extracted from the NRIM (presently NIMS) Japanese databases, see [12] for the relevant datasheet numbers. For these experiments, performed on steels in annealed state, the instantaneous

strain upon loading was calculated by Equation (1) with a yield strength of 100 MPa and a m_e= 0.5 and C'=750, 590, and 440 MPa at temperatures of 550, 600, and 650°C.

Notably, according to [13], the precipitation of nitrides and carbonitrides for a nitrogen content of 0.07% and carbon content of 0.03% is significantly limited, even after 9200 hours at 650°C, while intragranular carbides are already present. The minimum creep rates from the current study almost align with the data referenced in [12]. The overlap of the two families of creep data is nearly complete, except for the tests conducted under lower stress conditions in this study.

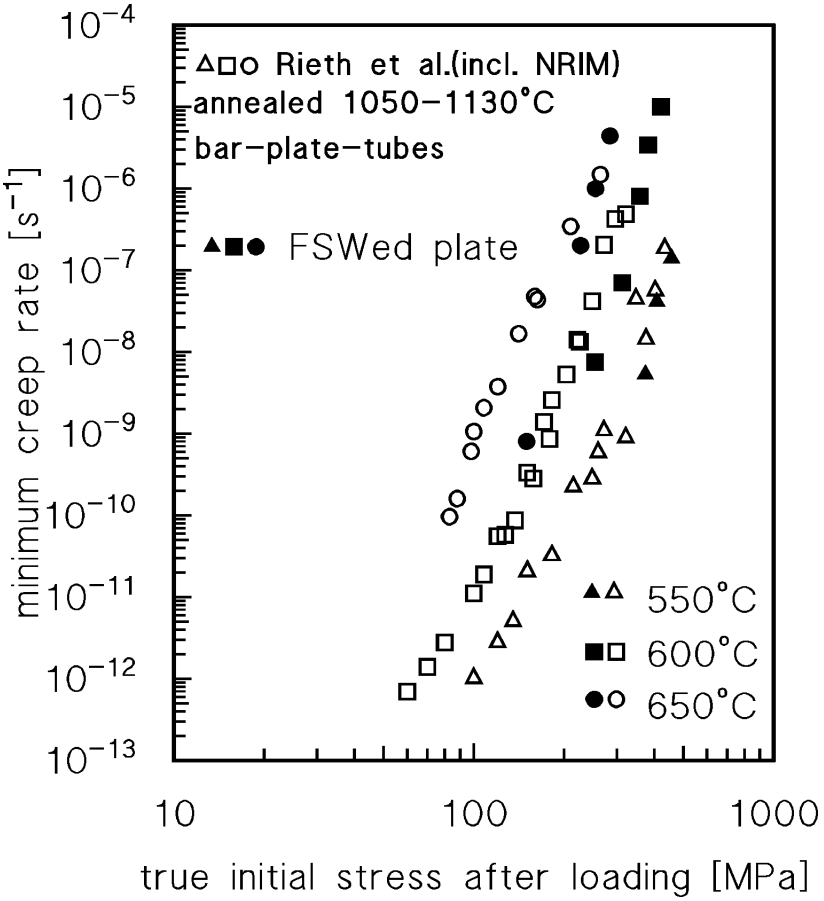
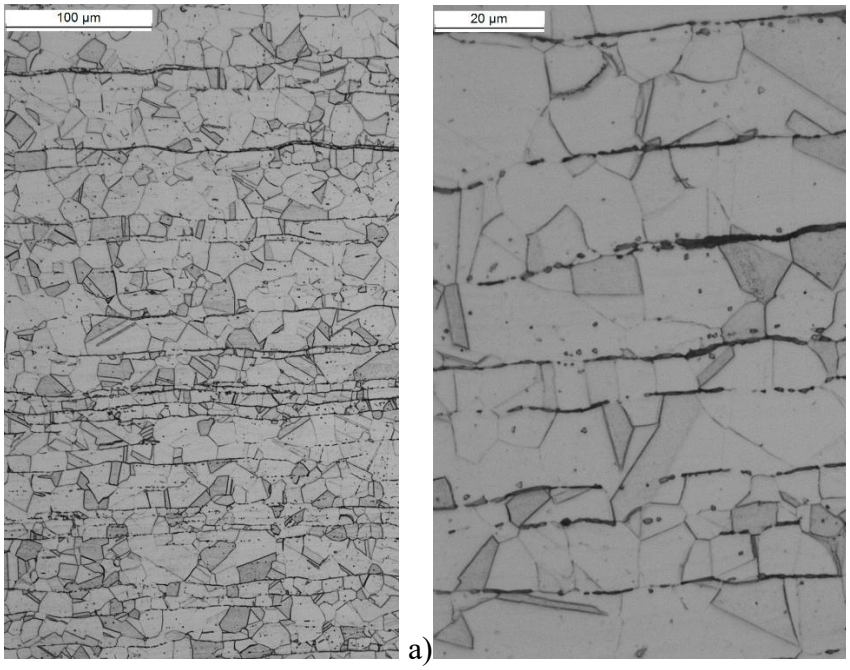


Fig.11 The Figure explores the correlation between the minimum creep rate and the true stress after loading for AISI 316L and for FSWed material. The true post-loading applied stress was calculated by Equation (1), with parameters C' set at 625, 500, and 450 MPa for temperatures of 550, 600, and 650°C, respectively, and m_e=0.3 and 0.38. Additionally, the data for 316L and 316 sourced from [12], which also encompasses various experiments from the NRIM (NIMS) Japanese database, are also reported. The nominal stress values documented in [12] were converted to true post-loading applied stress again using Equation (1), but with parameter C' set at 750, 590, and 440 MPa for temperatures of 550, 600, and 650°C, respectively. These values provide higher instantaneous strains, more in line with the mechanical response of an annealed steel

3.3 Microstructure after creep

Figure 12 presents the microstructure of a crept FSWed sample (650°C–240 MPa, CLE8) observed under optical microscopy in the nugget zone. At this low magnification, the internal microstructure appears virtually unchanged from its initial FSWed state. However, the increased reactivity of the grain boundaries to chemical etching suggests that a moderate degree of intergranular carbide precipitation may have occurred.

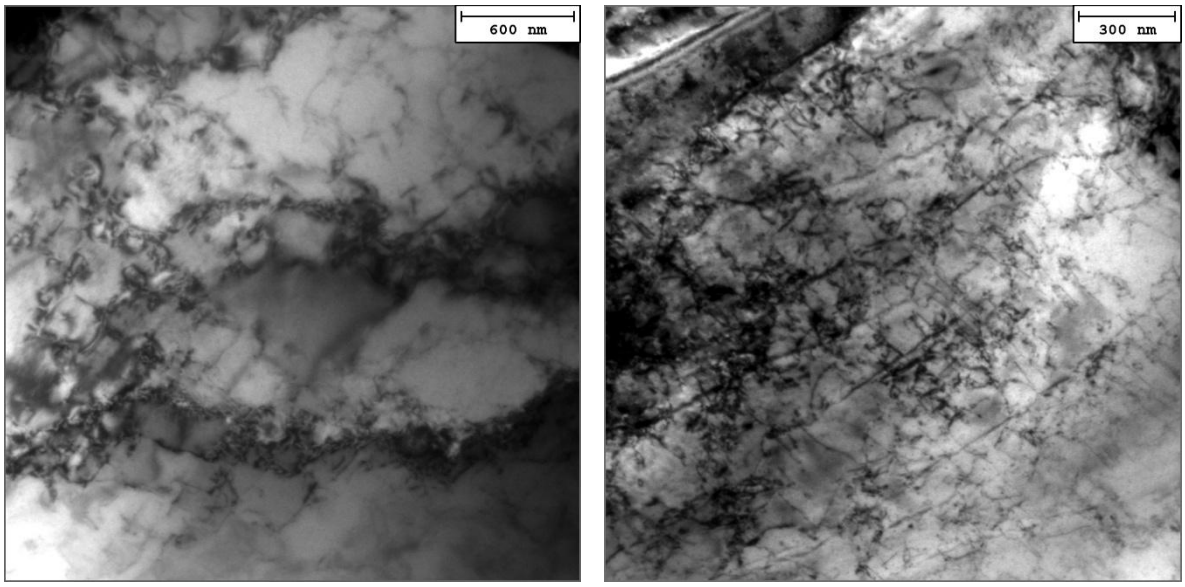


a) b)

Fig.12 Microstructure of the FSWed material (nugget zone) after creep (650°C–240 MPa, CLE8)

Figures 13a and 13b present representative TEM micrographs illustrating the typical microstructure under the 250 MPa and 250–350 MPa experimental conditions, respectively. No significant differences were observed between the two conditions. The microstructure primarily consists of tangled dislocations that do not appear fully organized into cell structures. More specifically, the tangled dislocations within the grains of the sample crept at 600°C- 250 MPa (CLE3), as well as those in the sample crept at 550°C, 250–350 MPa (VLE3), just show a tendency to form cell structures, more apparent in case of the test carried out at the highest temperature. However, a fully developed and well-organized cell network is not yet evident. The density of these dislocations is

higher than that observed in uncrept conditions. Additionally, both the crept samples still exhibit numerous twins extending from boundary to boundary within the austenite grains, similar to those observed in both the FSWed and uncrept samples. No significant precipitation was observed for these tests either too short (CLE3) or carried out at too low temperature (VLE3) to observe extensive formation of intragranular carbides.



a) b)

Fig.13 Representative BF-TEM showing the microstructure of the AISI 316L FSWed nugget crept at: a. 600°C, 250 MPa, and b. crept at 550°C, 250-350 MPa

4. Discussion

4.1 A physically based constitutive model: the steel tested in an annealed state

To contextualize the differences in the creep response of similar AISI 316 and 316 L steels with different initial microstructures, it is particularly useful to derive a description of the behaviour of the annealed material. After heat treatment, such a material has a microstructure that is practically free of dislocations and fully recrystallized.

The model presented here offers a streamlined derivation of the constitutive equations initially formulated by Sandström [14-19]. This model is based on the Taylor equation, rewritten in the form

$$\sigma \approx \sigma_{ss} + \sigma_p + \sigma_d + \sigma_w = \sigma_{ss} + \sigma_p + \alpha m G b \sqrt{\rho_f} + 0.62 \alpha m G b \sqrt{\rho_w} \quad (2)$$

where m is the Taylor factor, ρ_f and ρ_w are the dislocation densities in the cell interiors (free dislocations) and in the walls (averaged to the volume of the cell) respectively, G is the shear modulus, α=0.19 [20], b is the length of the Burgers vector (2.5×10^{-10} m), σ_{ss} is the solid solution hardening term. The equation $\sigma_d = \alpha m G b \rho_f^{1/2}$ describes the phenomenon of dislocation hardening. The strengthening contributions from particles and dislocations within the cell walls are represented by the terms σ_p and $\sigma_w = 0.62\ \alpha m G b \rho_w^{1/2}$ [19, 21]. The corrective term 0.62 in the last term of Equation (2) was introduced by considering that the dislocation spacing in the wall is one order of magnitude lower than in cell interiors (Sandström [19] used the value 0.5 in his analysis, see also [21] for further details). It is important to note that in the original formulation, Sandström and colleagues suggested that only a portion of the total dislocation density in the cell walls—specifically, the unbalanced dislocations—contributes to the back stress σ_w. These dislocations are unaffected by recovery mechanisms, which typically result in the annihilation of other dislocations present in the walls. Due to the challenges in identifying the specific nature of dislocations stored in the cell walls after deformation at elevated temperatures, this study will not differentiate between the various types of wall dislocations, thus assuming that recovery has already annihilated the other dislocation groups during heating and soaking.

The evolution of dislocation density during straining can be expressed as [14, 15]

$$\frac{d\rho_f}{d\varepsilon} = \frac{m}{bL} - \omega \rho_f - \frac{1}{\dot{\varepsilon}} M_{cg} G b^2 {\rho_f}^2 \quad (3)$$

where M_{cg} is the dislocation mobility and L means the dislocation mean free-path, i.e. the distance travelled by a dislocation before it undergoes a reaction, and ω is a constant. At high temperature the second term ($\omega\rho_f$) at the right side of Eqn. (3) is negligible when compared with the third term, and for this reason it will be not considered.

In general terms, it is here assumed that

$$\frac{1}{L} = \frac{C_L}{\sqrt{\rho_f}} + \frac{1}{L_p} + \frac{1}{L_w} \quad (4)$$

where C_L is a strain-hardening constant, L_p is the interparticle distance, L_w is the distance between cell walls, i.e. the dislocation-cell size.

Dislocation mobility in solid solution alloys can be written as [18]

$$M_{cg} \cong \frac{D_{0L}b}{kT} exp\left(\frac{\sigma_d b^3}{kT}\right) exp\left\{-\frac{Q_L}{RT}\left[1-\left(\frac{\sigma_d}{R_{max}}\right)^2\right]\right\} exp\left(-\frac{U_{ss}}{RT}\right) \quad (5)$$

where k is the Boltzmann constant, T is the absolute temperature (K), R is the gas constant, R_{max} is here quantified as 1.5 times the ultimate tensile strength (*UTS*) at the testing temperature, D_{0L}=3.15x10^{-4} m^2 s^{-1} and Q_L=293 kJ mol^{-1} [17]. The U_{ss} term represents the energy required for solute atoms to jump in and out of the solute clouds surrounding dislocations. For the elements Cr, Ni, Mo, Si, and Mn, the estimated U_{ss} values are 0.96, 0.46, 10, 2.2, and 2.9 kJ mol^{-1}, respectively [20]. Consequently, U_{ss} is equivalent to the highest of these values, which is 10 kJ mol^{-1} in the case of Mo-containing AISI 316.

The solid solution strengthening term is here expressed as

$$\sigma_{ss} = \alpha_{ss}(\sigma - \sigma_p - \sigma_w) \quad (6)$$

being α_{ss} a constant. The value α_{ss} =0.4 will be used in the following [4].

4.2 The interparticle distance L_p and the particle strengthening term

The particle-strengthening term is assumed to be equivalent to the Orowan stress (σ_{Or}), calculated, for a volume fraction f of particle size d, as

$$\sigma_p = \sigma_{Or} = 0.84\frac{mGb}{4\pi L_p\sqrt{1-\nu}} ln\left(\frac{d}{2b}\right) \quad (7)$$

where the interparticle distance is [4]

$$L_p = \frac{d}{2\sqrt{6f/\pi}} - d\sqrt{\frac{2}{3}} \quad (8)$$

4.3 Cell/subgrain size L_{sub}

The widely used formulation of the cell/subgrain size dependence on applied stress has the form

$$L_w = Kb\left(\frac{\sigma}{G}\right)^p \quad (9)$$

where, in most cases, p = -1 [22], although il could range between 0.05 and ≈2 (see [23] for a detailed discussion on this aspect), and K=10-20 [21, 24].

Figure 14 presents a compilation of experimental data for austenitic stainless steels sourced from various references [25-28]. Additionally, Table 2 provides a selection of information regarding the substructures of austenitic stainless steel after straining within the temperature range of 550 to 650°C. The broken lines in Figure 14 delineate the regions where either cells or subgrains were observed, and the intermediate transition region [29]. Apart from one single exception, from Michael et al., mainly cell arrangements were noted below 700°C, at least for short test durations. Furthermore, the AISI 301 samples, which were pre-strained up to 10% at 600°C [28], are not depicted in Figure 14 but are included in Table 2; these samples exhibited a well-defined cell substructure with L_{sub} measuring between 300-400 nm. The figure also illustrates the curve derived from Equation (1) with K=15, which offers a reasonably accurate representation of the results. Although the data from Michael et al. [26] deviates from the curve in the intermediate stress range, where it tends to overestimate the cell size observed in more recent studies [28, 30], the formulation with K=15 will be employed in subsequent analyses. For clarity, it is important to note that a weaker stress dependence of L_w on the applied stress, such as p=0.5, may more accurately characterize the variation in cell size with σ/G, as has been sporadically reported in the literature for other materials [29].

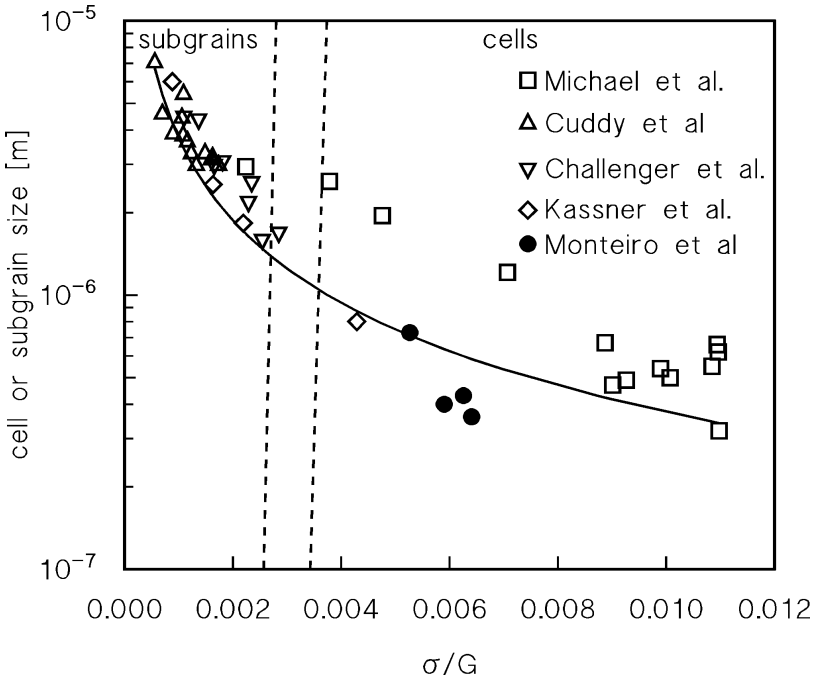


Fig.14 Subgrain/cell size as a function of adimensional stress for austenitic stainless steels [25-28]. The curve was obtained by Equation (9), with K=15. The dashed lines identify the regions were subgrains and cells form, as given in [29], and the intermediate transition region

Table 2. Summary of literature quantitative data on cell formation in austenitic stainless steels.

steel	strain rate	temperature	strain	Qualitative analysis	Quantitative data	source
AISI301	$3.5X10^{-5}$ s^{-1}	500°C	2%	discernable cells	n.a.	Monteiro et al. [30]
			22%	cell structure	Lw=0.4 μm $\rho_w \approx 10^{15}$ m^{-2}	
			29%	cell structure	Lw =0.43 μm $\rho_w \approx 10^{15}$ m^{-2}	
		600°C	5%	discernable cells	n.a.	
			15%	cell structure	L_w =0.73 μm $\rho_w \approx 10^{14}$ m^{-2}	
			32%	cell structure	L_w =0.36 μm $\rho_w \approx 10^{15}$ m^{-2}	
AISI301	$5.0x10^{-4}$ s^{-1}	600°C	5%	discernable cells	n.a.	Peng et al. [28]
			10%	cell structure	L_w ≈0.3 μm	
AISI316	$2.7x10^{-5}$ s^{-1}	593°C	31%*	cell structure	L_w =0.67 μm	Michel et al. [26]
		650°C	20%*	subgrain structure	L_w=1.21 μm	

*uniform strain

4.4 Dislocation density in cell/subgrain walls ρ_w

In general, the rearrangement of dislocations within subgrain walls is prevalent in low-stress/high-temperature conditions, whereas cell formation occurs under high-stress/low-temperature scenarios.

Mathew and colleagues [8], on the other hand, noted the simultaneous occurrence of elongated subgrains and uniformly distributed dislocations interacting with carbides across different grains following creep at 600°C. At 550°C, the propensity for cell formation was clearly observable in the high-stress regime, while at lower stress levels, dislocations formed loose tangles alongside a significant presence of carbides. At this temperature, extended exposure may thus promote precipitation effects, a phenomenon that is unlikely to manifest at 500°C.

The correct estimation of the dislocation density in the cell/subgrain boundaries is a complex problem. Few data on ρ_w available for stainless steels are shown in Figure 15 [30, 31]. Sikka and co-workers calculated the dislocation density in subgrain walls by the well-known Equation

$$\rho_w = \frac{3\theta}{bL_w} \tag{10}$$

where θ is the average subgrain misorientation and L_w is the subgrain size. This formulation provides the dislocation density averaged over each cell with a volume of L_w^3. Thus, the total dislocation density can be simply obtained as

$$\rho_{tot} = \rho_w + \rho_f \tag{11}$$

Monteiro and colleagues measured the dislocation density using the traditional intercept method. If we consider the cell/subgrain as a soft zone surrounded by a hard case (the wall), the dislocation density could be expressed as [32]

$$\rho_{tot} = f_w\rho_h + (1 - f_w)\rho_s \tag{12}$$

where f_w is the cell walls volume fraction, being ρ_s and ρ_h the dislocation density in a volume of cell interior and wall respectively, not averaged in a L_w^3 volume. This fact implies that [33]

$$\rho_S = \frac{\rho_f}{1-f_w} \tag{13}$$

and

$$\rho_h = \frac{\rho_w}{f_w} \tag{14}$$

Monteiro and colleagues provided an estimate of ρ_h, which should be compared with the values reported in [31]. To facilitate this comparison, the values need thus to be multiplied by a factor f_w. The authors acknowledged that the relatively low precision in measuring fuzzy tangles resulted in values that were reported within one order of magnitude. Despite this uncertainty, the dislocation density in the cell walls remains significantly above the straight line with a slope close to 1, which characterizes the ρ_w dependence on adimensional stress for the subgrains discussed in [31]. Thus, the equation

$$\rho_w = \beta \frac{\sigma}{G} \tag{15}$$

with $\beta \approx 3\text{x}10^{16}$ m^{-2} for the data above at T>700°C (β_{min}) will be used to relate the wall-dislocation density to applied stress in correspondence of the minimum creep rate. The total dislocation density observed in a wrought AISI 304L, subjected to a tensile strain of 32% at room temperature, leading to the development of fine dislocation walls, was measured at 2.8 x 10^{15} m^{-2} [34]. If one assumes that density $\rho_w \approx 4\rho_i$, then $\rho_w \approx 2$ x 10^{15} m^{-2}. With $\sigma \approx$ 535 MPa (from the curves in [34]), Equation (15) gives $\beta \approx 2.9$ x 10^{17} m^{-2}. Let one suppose that below 400°C the β parameter remains constant (β_{max}), its variation with temperature between 400 and 700°C could be empirically described by an equation in the form

$$\beta = \beta_{min} + \frac{\beta_{max} - \beta_{min}}{1 + exp\left[-c_\beta\left(1/T - 1/T_{50}\right)\right]} \tag{16}$$

where $1/T_{50}$ is the inverse of the absolute temperature at which β=1.6 x 10^{17} m^{-2} and c_β is a constant. Figure 15 shows the calculated variation of η with $1/T$, with c_β=2.5x10^4 K and $1/T_{50}$=1.2 x 10^{-3} K^{-1}. This curve gives, for the AISI 301 steel in the experimental conditions investigated by Monteiro et al. [30], $\rho_w \approx$ 1.7x10^{15} and 5.3x10^{14} m^{-2} at 500°C and 600°C, after straining up to 29 and 32% respectively. The authors previously indicated that for both conditions, the suggested value is ρ_h = 10^{15} m^{-2}, an estimation provided within one order of magnitude due to experimental uncertainty. The values of 1.7 x 10^{15} and 5.3 x 10^{14} m^{-2} can be thus regarded as credible.

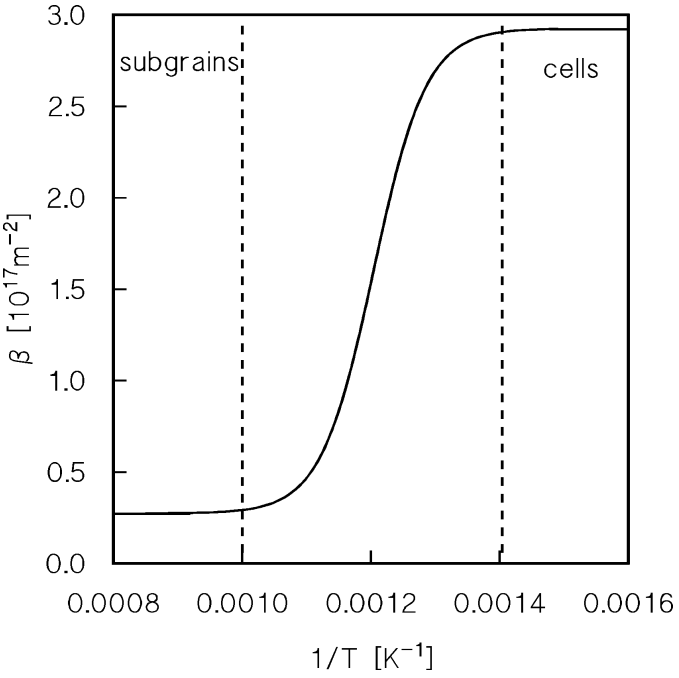


Fig.15 Variation of the β parameter with respect to $1/T$ in the transition regime between high temperatures, characterized by subgrain formation, and low temperatures, associated with cell formation

Despite being empirical, Equation (16) still holds significance as it illustrates the increase of wall dislocation density in the transition between subgrain boundaries, in general built up by one layer of dislocations, and cell dense walls, which have a finite width and are formed by tangled dislocations. This phenomenon might be attributed to the reduced efficiency of recovery mechanisms. The density denoted as ρ_w is averaged over the entire volume of the cell. An increase in the wall width (w) – i.e. in an increase of the volume fraction of hard boundary zones, f_w – results in a corresponding increase in ρ_w even in the case ρ_h remains relatively constant, Equation (14). According to Koneva et al. [35], the value of the coefficient η in the relationship

$$w = \eta L_w \tag{17}$$

valid in many fcc metals, decreases in Cu and Ni as the deformation temperature increases. An examination of the micrographs in [30] for AISI 301 steel, which was deformed to a strain nearing 30% at temperatures of 500 and 600°C, appears to substantiate this conclusion.

4.5 Description of the annealed steel response after precipitation of carbides: model P

A recent comprehensive examination of the literature reveals the critical role of carbides and carbonitrides in AISI 316 and 316L [4]. Precipitation is observed even during relatively brief testing periods at temperatures of 600 and 650°C and after longer durations at 550°C. The findings presented in reference [12] indicate that variations in carbon (C) content, ranging from 0.02% to 0.07%, and nitrogen (N) content, from 0.019% to 0.08%, do not significantly affect the creep response of the steel. It can be then supposed that particles – mostly intragranular carbides- significantly influence the creep behavior of the steel. These particles hinder dislocation mobility, delaying the development of cells and subgrains. Consequently, with a finely distributed array of precipitates, the dislocation distribution remains relatively uniform, resulting in a scarcity of cells or subgrains [8, 11, 36]. Thus, $1/L_w \approx 0$. In addition, it can be assumed that $L_p << L_d$ (the correctness of this assumption will be verified in the following). Thus

$$\frac{1}{L_p} \approx \frac{1}{L} \tag{18}$$

At steady state, combination of Eqns. (9)-(18) gives

$$\dot{\varepsilon}_m = \frac{M_{cg} G b^3 L_p}{m} \left(\frac{\sigma_d}{\alpha m G b} \right)^4 \tag{19}$$

with

$$\sigma_d = \sigma - \sigma_{Or} - \sigma_{ss} = (1 - \alpha_{ss})(\sigma - \sigma_{Or}) \tag{20}$$

The analysis of the microstructural information from [8] described in [4], gave $d_p \approx 83$nm f=0.8% after 2.2x10^3 h at 600°C under 195 MPa. Exposure for longer times (2.39x10^4 h under 155 MPa at the same temperature) did not cause substantial variation in d_p and f. The analysis of the micrographs presented in [8] for the samples tested at 550°C-215MPa for 5.4x10^4 h, and 650°C-145MPa for 800 h, gave $d_p \approx 55$ nm and 115 nm respectively. Taking $f = 0.8\%$ for all the considered temperature, calculation gives $\sigma_p \approx 98$, 71 and 51 MPa at the testing temperature (550, 600 and 650°C).

The R_{max} parameter, as above mentioned, is assumed to be equivalent to 1.5 *UTS* at the relevant temperature. Yet, the *UTS* is usually obtained in experiments of short duration, where precipitation is not expected to occur. Thus, to describe longer test data, it is here assumed that

$$R_{max} = 1.5\left(UTS + \sigma_p\right)\Big|_T \quad (21)$$

with *UTS*=437, 360 and 305 MPa at 550, 600 and 650°C [10]. Figure 16 shows the calculated curves, and the initial true stress *vs* minimum strain rates measured in this study and those collected in [12]. In the context of the longest tests conducted at temperatures of 600 and 550°C, as reported in reference [12], it is imperative to exercise caution when evaluating the accuracy of minimum creep rates less than 10^{-11} s^{-1}. This caution arises from the fact that all these low-stress experiments were terminated after a uniform duration of $8.5x10^4$ hours. For reference, it is noteworthy that a minimum strain rate of $1.9x10^{-11}$ s^{-1} observed in a test at 600°C, as indicated in [12], correlates to a rupture time of $1.5x10^5$ hours. For this reason, the Figure does not include data corresponding to strain rates below 10^{-11} s^{-1}.

The description of the experimental data is indeed excellent in the full range of five orders of magnitude of strain rate.

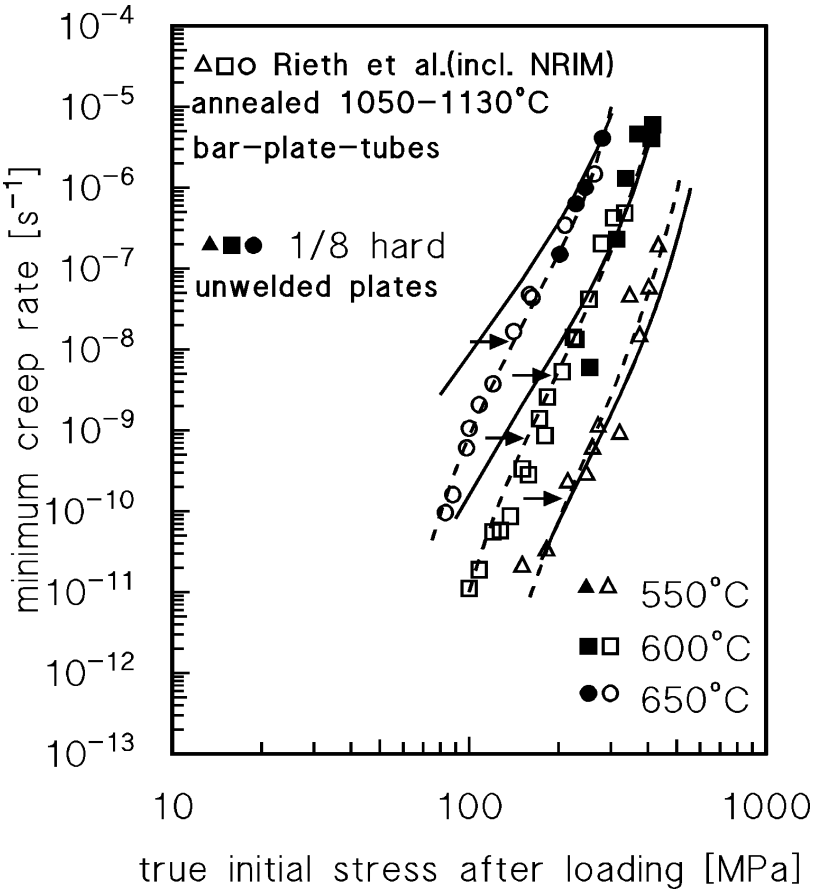


Fig.16 Calculated minimum creep rate dependence on applied stress for AISI 316 and 316L at 550, 600 and 650°C. The dashed lines represent the curves calculated by supposing that the dislocation free path corresponds to interparticle spacing obtained from [8] (model P). The arrows denote the experimental conditions, specifically stress and temperature, that are associated with the microstructural investigations referenced in [8]. These conditions are thus here utilized to assess the particle-strengthening effect in AISI 316. The solid line represents the curves calculated by supposing that precipitation did not occur, and that the dislocation mean free path was equivalent the cell diameter (model C). Open symbols from [12]

Figure 17 plots L_p and L_d as a function of nominal stress. The strain hardening constant was calculated as [24, 20]

$$C_L = \frac{K}{\alpha m} \tag{22}$$

which gives $C_L \approx 25$. Then

$$L_d = C_L \frac{\alpha m G b}{\sigma - \sigma_w - \sigma_{ss}} \tag{23}$$

which, ad clearly shown in Figure 17, is by far larger than L_p. Should any cell/subgrain form for sufficiently long time of exposure, Equation (9) invariably gives $L_w >> L_p$.

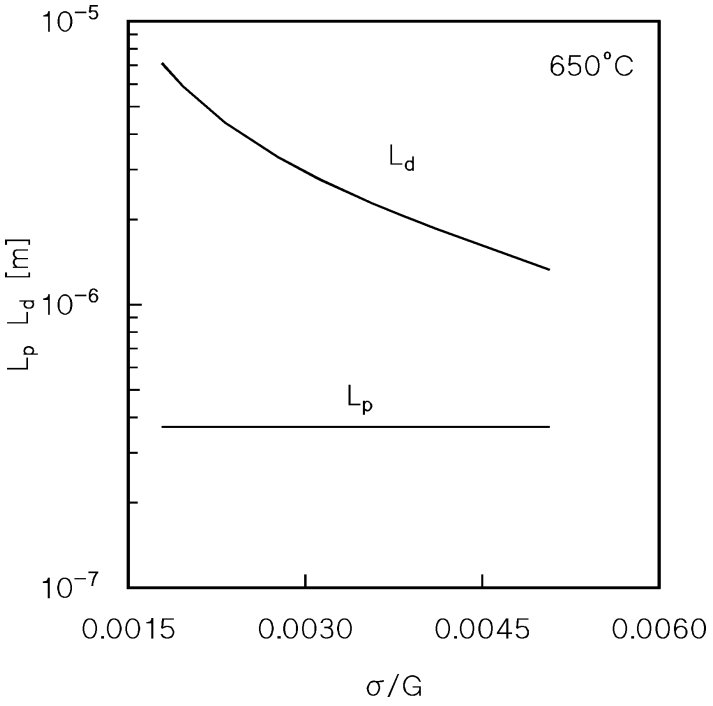


Fig.17 Comparison between L_p and L_d at 650°C. The basic assumption in this case was that the dislocation mobility was severely restricted by intragranular particles, leading to a retarded formation of cells/subgrains, i.e. $1/L_w \approx 0$. The situation is similar at 550 and 600°C. The assumption $L_d >> L_p$ is confirmed

The model's accuracy in characterizing the minimum creep rate as a function of applied stress is quite remarkable, especially considering that it also accounts for the effects of precipitate dispersion under experimental conditions where precipitation is not anticipated due to the short duration of the tests. This observation is particularly relevant for the experiments conducted in this study at 550°C. The subsequent section will address this issue in greater detail.

4.6 Description of annealed steel response in absence of precipitation; model C

In the extremely high-stress regime examined in this study, significant plastic strains develop immediately upon loading. Typically, this is associated with the formation of dense dislocation walls prior to creep [18, 30]. In the absence of any precipitation, a predictable scenario in the high

stress regime, particularly at temperatures of 550 and 600°C, i.e. $1/L_p$ approaches zero. In this context, it can be assumed that L_w is much less than L_d. The correctness of this assumption will be again verified in the following.

At steady state, now combination of Eqns. (9)-(18) gives

$$\dot{\varepsilon}_m = \frac{M_{cg} G b^3 L_w}{m} \left(\frac{\sigma_d}{\alpha m G b} \right)^4 \tag{24}$$

with

$$\sigma_d = \sigma - 0.625 \alpha m G b \sqrt{\rho_w} - \sigma_{ss} = (1 - \alpha_{ss}) \left(\sigma - 0.625 \alpha m G b \sqrt{\rho_w} \right) \tag{25}$$

In this case, R_{max} was calculated directly as 1.5 *UTS* at the relevant temperature. The curves obtained in the high-stress regime with the L_w and ρ_w values calculated as in the previous section, are also shown in Figure 16. The model curves effectively represent the high-stress creep results at temperatures of 550 and 600°C. However, they begin to diverge at 600°C from experimental data as the stress levels decrease and exposure time increases. At the highest temperature, when precipitation is greatly accelerated, the model curve obtained by considering the particle-strengthening effect provides a better description.

Figure 18 shows a comparison between L_d and L_w. The correctness of the assumption $L_d >> L_w$ is confirmed.

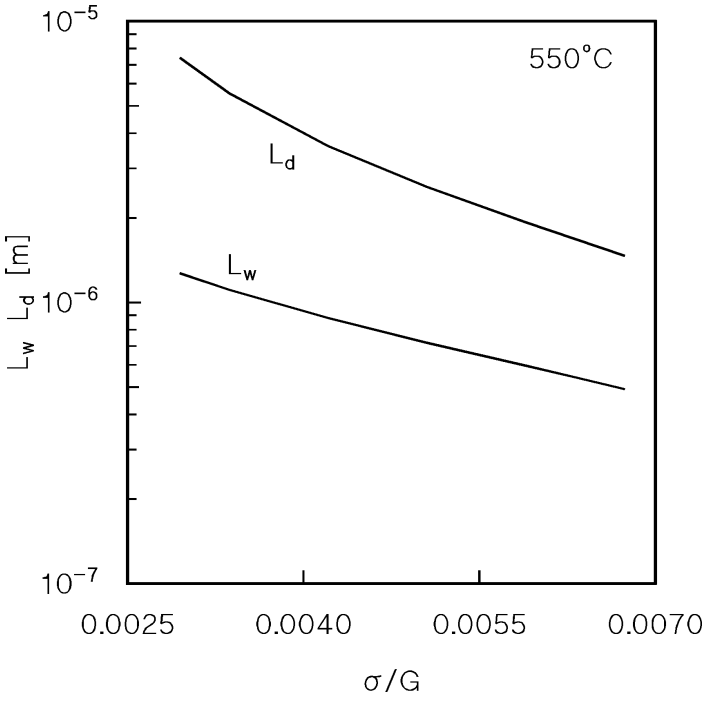


Fig.18 Comparison between L_d and L_w in absence of any intragranular precipitation, i.e. $1/L_p \approx 0$ at 550°C. The situation is similar at 600 and 650°C. The assumption that $L_d >> L_w$ is confirmed

4.7 Description of the annealed material response at lower temperatures by model C

An intriguing topic for discussion is the potential to extrapolate the results of the model to lower temperatures, where precipitation occurs only after very long times. Unfortunately, existing studies in the literature have consistently focused on the creep response of AISI 316 or 316L at temperatures of 550°C and higher. Only one of the experiments listed in [12], has been conducted under an applied stress of 400 MPa for a duration of 5308 hours, yielding a minimum creep rate of 1.33×10^{-9} s^{-1}. Another test was conducted by other authors at 325 MPa and interrupted after 15.226 hours, which yielded a minimum strain rate of 2.4×10^{-11} s^{-1} [37]. Additionally, Brinkman [38] provided further data from creep tests performed on AISI 316, which were interrupted after durations spanning from 35,000 to 40,000 hours.

The relatively low temperature suggests that the neglection of the second term at the right-hand side of Eqn.(3) could result in underestimation of the strain rate. Without neglecting the $\omega\rho_f$ term, the model equation becomes:

$$\dot{\varepsilon}_m = \frac{M_{cg} G b^2}{\frac{m}{bL_w} - \omega \left(\frac{\sigma_d}{\alpha m G b}\right)^2} \left(\frac{\sigma_d}{\alpha m G b}\right)^4 \qquad (26)$$

with ω=15 [21]. Calculations using the β-value obtained from Eqn. (16) with *UTS* of 450 MPa, give the plot shown in Figure 19. The model provides a reasonably accurate description of the minimum creep rate dependence on applied stress.

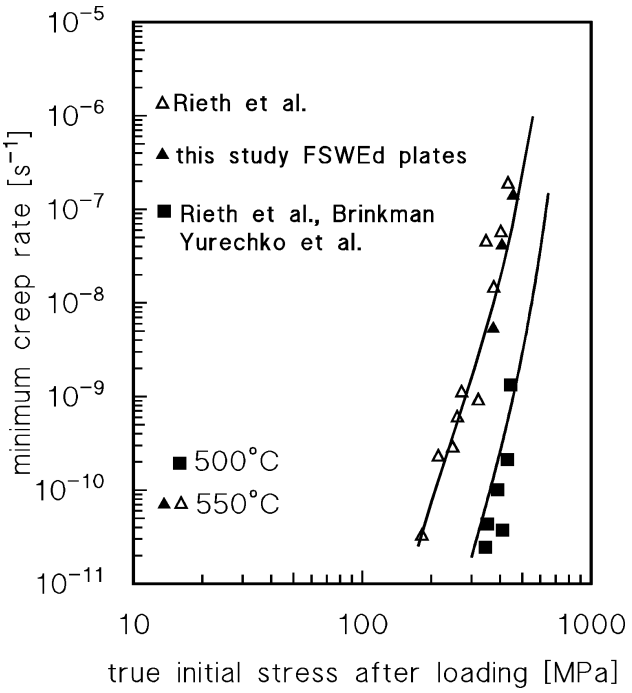


Fig.19 Calculated minimum creep rate dependence on applied stress for AISI 316 at 500°C. The symbol represents the single test at 500°C from [12, 37, 39]. The instantaneous strain after loading at 500°C was calculated by Equation (1) with R_y=100 MPa, C = 900 MPa and m_e=0.5. The experimental data collected at 550°C are presented for comparative analysis. The curves illustrate the relationship between the minimum creep rate and the applied stress, based on the assumption that the dislocation mean-free path is equivalent to the cell size, without considering precipitation effects (model C)

4.8 Critical discussion of the model for creep of annealed steel: physical plausibility

The analysis indicates that the mid- and long-term creep behavior of the AISI 316 and 316L is predominantly affected by the formation of intragranular carbides at temperatures of 600 and 650°C. At these elevated temperatures, precipitation within the grains is anticipated to occur after 500 and 50 hours, respectively [12]. The presence of a finely dispersed particle distribution leads to

a reduction in the dislocation free path and introduces back stresses due to the interaction between dislocations and particles (model P). By contrast, in lower temperature conditions or during brief exposure periods, especially when significant precipitation is minimal, the dislocation free path is predominantly affected by the rearrangement of dislocations at cell boundaries (model C). At 600°C, precipitation is negligible during very short exposure times, allowing the formation of cell walls to dictate the dislocation free path.

The behavior can be effectively characterized by the set of constitutive equations presented in the preceding sections. Figure 20 thus compares the available experimental data with the curves obtained by combining model P and model C in the lower and higher stress regimes respectively.

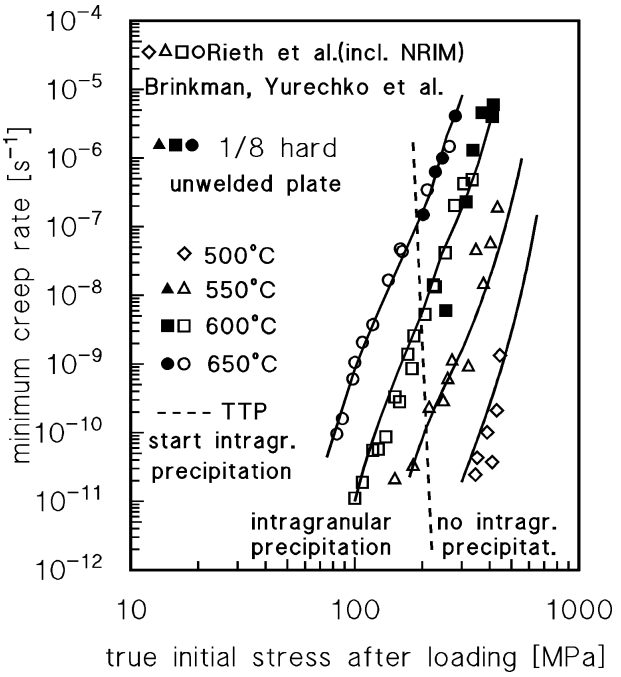


Fig.20 Combined curves for models C and P: a) model compared with available experimental data reported in Figures 16 and 19(AISI 316 and 316L). The dashed line indicates the start of precipitation according to the TTP diagram for AISI 316 L reported in [12], and based on the NRIM Metallographic Atlas for long term Crept materials No- M-2. The minimum strain rate value corresponding to the time t_s for starting intragranular precipitation was estimated as $(2.8\text{x}10^{-4}/t_s)^{1.355}$ [4]

The figure illustrates a broken line that denotes the initiation of intragranular precipitation [12]. The time is converted into strain-rate based on an empirical relationship proposed in [4]. Consequently,

this line delineates the conditions under which the precipitation of intragranular carbides commences during the minimum creep rate range. The comparison between the broken line and the arrows in Figure 20 suggests that the TTP diagram from NRIM Metallographic Atlas for long term Crept materials No- M-2, as presented by Rieth et al., provides a significantly higher initiation time for intragranular precipitation than the experimental evidence obtained from AISI 316 with 0.05% C. This fact could be related to the different C content, but, on the other hand, creep data summarized in [12] align on the same curves irrespective of the C content, varying from 0.02 to 0.08%. Thus, the minimum creep rates for AISI 316L quite closely align on the curves obtained with considering the precipitation of intergranular carbides in a standard AISI 316.

The model here presented is fundamentally based on a simplified representation of the underlying physics of the phenomena. In the case of model P, as previously noted in [4], the characteristics of precipitate dispersion exhibit significant variations over time. Consequently, the notion of a constant strengthening contribution across the entire range of test durations at a specific temperature is, at best, an unrealistic assumption. On the other hand, the comprehensive analysis presented in [4] indicates that when considering the kinetics of precipitation and the coarsening of precipitates, the alterations in the model curves remain relatively modest.

In the context of model C, this analysis refrains from the overly ambitious goal of delivering a conclusive explanation regarding the role of substructures. Notably, it diverges from established literature by emphasizing the necessity of incorporating temperature dependence into the cell-wall dislocation density averaged on the cell volume. This adjustment arises from the significant disparities in wall dislocation density noted at elevated temperatures, where the grain-interior sub-units take on the form of subgrains, in contrast to low temperatures, where the cells exhibit dense dislocation boundaries. The inquiry thus emerges regarding the compatibility of the calculated values of microstructural parameters, specifically cell size and dislocation density, with the experimental evidence presented in prior studies.

Figure 21 delineates the correlation between the calculated cell size and the total dislocation density at the minimum creep rate, juxtaposed with the data documented in [40] and derived from historical references [41-44]. In addition, also data from [45] are included in Figure 21a. The data reasonably supports the phenomenological relationship, indicated by a slope nearing -1, between cell size and the square root of the total dislocation density as suggested by Holt [46]. The calculations of this study at temperatures of 600 and 650°C demonstrate a good correlation with the data for AISI 316 referenced in [45], which pertains to subgrains developed at temperatures exceeding 700°C. Figure 21b presents data exclusively from [45], detailing the cell and subgrain sizes calculated under both high (model C) and low (model P) stress regimes at 650°C. This analysis assumes that these substructures can form even in the presence of a diffuse precipitation, a premise that is likely valid primarily for extended testing durations. Notably, the two datasets exhibit considerable overlap.
At 550°C, the total dislocation density for AISI 316L, as per model C, is somewhat higher, a fact attributed to the increased fraction of dislocations entangled within thicker walls. Notably, the cells observed in copper by Staker et al. [40] exhibit significantly thinner walls, contrasting sharply with the denser dislocation walls identified in AISI 316 [47].

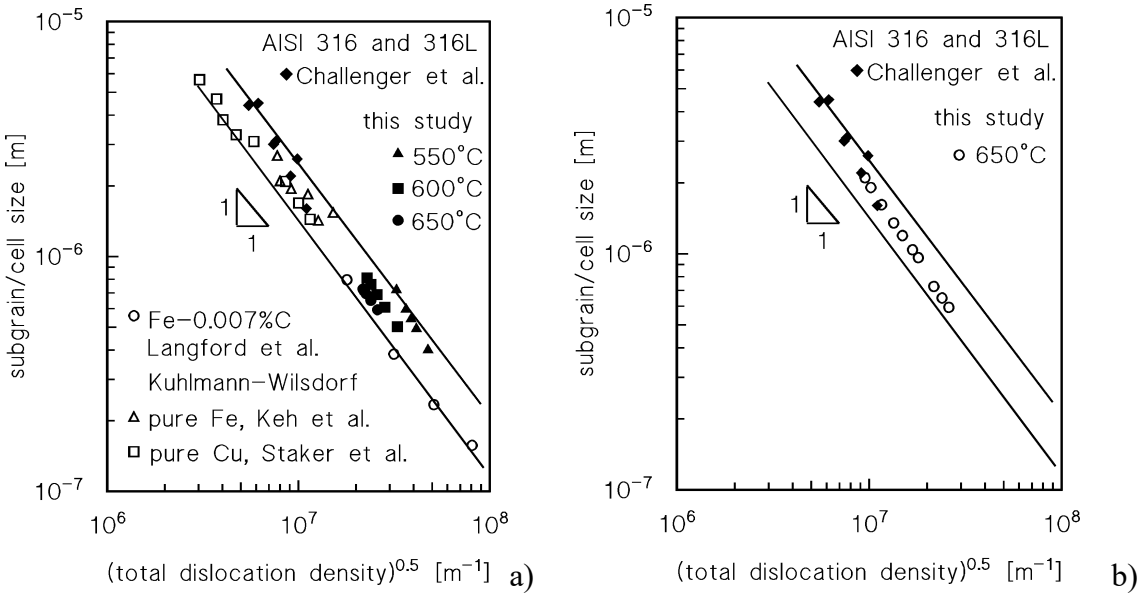


Fig.21 Cell/subgrain size as a function of the total dislocation density calculated for various stresses: a) in the regime where the dislocation mean free path corresponds to cell size (model C),

compared with literature data from [40- 45]; b) at 650°C in the whole range of applied stress of Figure 20, based on the assumption that substructures form at this high temperature also in presence of precipitates where model P is applicable, compared with AISI 316 data from [45]

The final aspect that warrants a concise discussion is the distinction between AISI 316L stainless steel, a low stacking-fault energy material, and aluminum, in which the formation of subgrain at steady state is a common feature. The original Sandström model is applicable for modeling the creep response of aluminum [48] and aluminum-magnesium alloys [49] without accounting for the influence of dislocation sub-boundaries. In the case of aluminum-magnesium alloys, this phenomenon can be elucidated by recognizing that magnesium, which is said to reduce the stacking-fault energy, significantly inhibits or retard the formation of subgrains, which are typically prevalent in high stacking-fault energy pure aluminum. Conversely, the omission of the effects of subgrain formation in pure Al [48] suggests that the strengthening contribution of these boundaries may be significantly less critical compared to that of cell walls. This observation is consistent with previous analysis by Kassner [50-52], who concluded that in AISI 304 (and aluminum) strained at high temperature, only the density of dislocations within the subgrain interior is associated with the rate-controlling process for five-power-law creep-plasticity. Cells are delineated by broad and diffused boundaries that encompass dislocation tangles, whereas sub-boundaries exhibit a much narrower and well-defined structure [29]. If such is the case, the straightforward conclusion is that the thin subgrain walls play a negligible strengthening role. On the other hand, even the dense dislocation walls surrounding the cells are not impenetrable. Dislocations can traverse more than one cell before becoming immobilized [53]. The assumption $L=L_w$ in this study is predicated on the notion that the dislocation-free path represents the average distance before a reaction, that is, between two nearest obstacles, which are not insurmountable. Dislocations have the capability to pass both particles and cell boundaries; however, this process requires an elevation in stress, which is represented by the σ_p or σ_w parameters.

4.9 The effect of Friction Stir Welding on creep response

The comprehensive constitutive analysis presented in the preceding sections leads to significant conclusions regarding the influence of Friction Stir Welding on the creep behavior of AISI 316L. Notably, FSW induces a modest enhancement in both hardness and strength within the welded joint compared to the unwelded plate of the present study. However, it is important to note that the unwelded plate, being in a 1/8 hard state, is already harder than annealed steel.

When analyzing the magnitude of instantaneous strain during loading—noticeably greater in the unwelded plates—the creep responses of both the FSWed and parent materials in the very high-stress regime exhibit remarkable similarities, particularly in the dependence of the minimum creep rate on applied stress. In this regard, their behavior only marginally differs from that of annealed steel. However, the response changes when the applied load is reduced: in this case, the minimum creep rates drop by at least an order of magnitude compared to those of annealed steel tested at 600 and 650°C (Figure 22).

These preliminary results suggest that the initial strain-hardened microstructure plays a key role in determining the creep response of the FSWed material. In annealed steel, microstructural evolution is primarily governed by the interplay of applied stress, temperature, and time, leading to the activation of various strengthening mechanisms—such as cell boundaries or particles acting as obstacles to dislocation motion. In contrast, the initial microstructure of the FSWed material already exhibits a high density of twins and a relatively elevated dislocation density. Twins contribute to strengthening the steel by impeding dislocation motion due to the slip discontinuity caused by their mirror symmetry [54]. Even cell formation is somewhat delayed, due to the reduced dislocation mobility. Since twins remain clearly discernible even after creep exposure, it is reasonable to conclude that this strengthening effect remains active across the entire range of experimental conditions here investigated. Additionally, the concurrent action of moderate intragranular precipitation may provide further strengthening, particularly in the test conducted at 650°C and 150 MPa for over 900 hours. In contrast, in the high-stress regime, the high applied loads generate in the

annealed steel a significant dislocation density, causing the microstructure to rapidly evolve into a 'strain-hardened' state which, mutatis mutandis, closely resembles that of the FSWed material. Consequently, under these conditions, annealed and FSWed steels exhibit no significant differences in behavior.

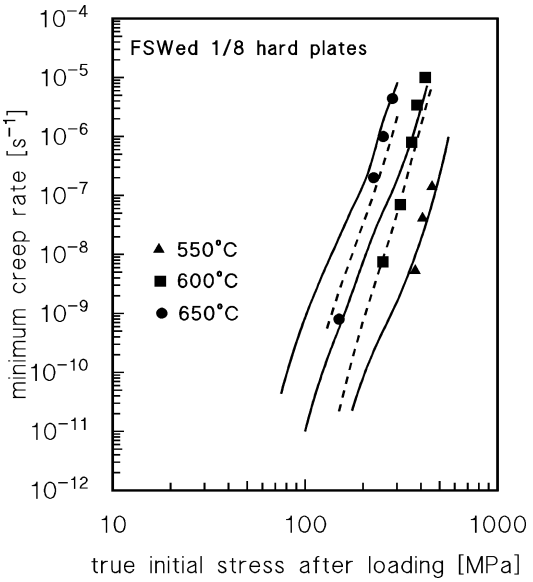


Fig. 22 Curves - C version of the model- for annealed steel compared with minimum creep rates for AISI 316L 1/8 hard plates after FSW. In this case, the values L_w = 200 nm, with σ_w = 110 MPa at 600°C and 80 MPa at 650°C were arbitrarily selected

If one assumes that twins are an important strengthening factor, an effective distance—dependent on grain size and twin thickness—could be introduced, allowing for the derivation of a Hall-Petch-type relationship for room-temperature strength [54, 55].

However, even the most sophisticated attempts [56] to model the strengthening role of twins at room temperature are not sufficient to accurately quantify their effect on the dislocation free path or the development of back stress during creep. As a result, the constitutive models described in the previous section cannot yet be properly adjusted to describe the creep response of FSWed AISI 316L without introducing empirically determined parameters through a best-fitting procedure. For instance, the two broken curves in Figure 22 were obtained by arbitrarily introducing, in the “C version” of the model, L_w = 200 nm and σ_w = 110 MPa at 600°C and 80 MPa at 650°C. Here, the subscript *w* does not refer solely to cell walls but rather to the combined effect of obstacles

(dislocations, twin boundaries, etc.) already present at the beginning of the test. However, the simultaneous action of these various strengthening mechanisms, each introducing obstacles of varying strengthening effectiveness, presents a clear and currently still insurmountable challenge in quantifying the effective dislocation free path and the magnitude of the back stress.

The approach used for annealed steel may thus provide a reasonable description of the dependence of the minimum creep rate on applied stress, as well as a qualitative explanation of the behavior of FSWed austenitic stainless steel—where welding introduces various obstacles to dislocation motion, shortening the dislocation free path and generating back stress. However, the arbitrary selection of L_w and σ_w in FSWed material suggests only the potential suitability of the constitutive framework for describing the creep response of welded steel, rather than definitively validating it from a quantitative perspective for this specific case.

5. Conclusions

The creep response of Friction Stir Welded (FSW) AISI 316L stainless steel was investigated through short-term constant-load creep experiments at temperatures ranging from 550°C to 650°C. For comparison, a few experiments were also conducted at 600 and 650°C on the unwelded plate material, which was in a 1/8-hard initial state. The key findings of the study can be summarized as follows:

i. In the very high-stress regime, the FSWed steel exhibited minimum creep rates slightly lower than those measured in both the 1/8-hard and annealed states.

ii. As the applied stress decreases, the behavior of the FSWed steel deviates significantly from that of the same material in the annealed state. This difference can be attributed to the initial microstructure after FSW, which is characterized by an extensive presence of twins and a relatively high dislocation density.

iii. These differences in behavior correspond to distinct microstructural evolutions in the crept steel, depending on its initial condition. Literature evidence indicates that during

creep testing under high stresses in this temperature range, the microstructure of annealed steel evolves to form dislocation cells separated by thick boundaries. Only after sufficiently long exposure times, typical of lower stress experiments, does precipitation occur. The formation of fine intragranular carbides significantly hinders dislocation mobility, delaying the development of substructure. Eventually, subgrains form after prolonged exposure.

iv. The microstructural evolution differs in FSWed samples. In the short-term tests of this study, the "strain-hardened" initial microstructure remained sufficiently stable to result in lower minimum creep rates. This effect is less pronounced in the very high-stress regime, where large loads induce significant instantaneous plastic strains, leading to strain hardening even in the initially annealed microstructure.

v. A physically-based constitutive model was successfully applied to describe the creep response of the annealed steel, incorporating the distinct microstructural features mentioned above. While the same model provides a reasonable qualitative explanation of the creep behavior of FSWed steel, a quantitative description remains unattainable due to the lack of critical information regarding the contribution of the various concurrent strengthening mechanisms.

Acknowledgments

This research received no specific grant from any external funding agency in the public, commercial, or not-for-profit sectors.

Author contributions

Stefano Spigarelli: Conceptualization, Methodology, Investigation, Visualization, Validation, Formal analysis, Data curation, Writing-original draft.

Marcello Cabibbo: Methodology, Investigation, Writing-original draft.

Daniele Ciccarelli: Investigation, Data curation.

Alberto Santoni: Methodology, Investigation, Formal analysis, Data curation.

Michael Regev: Conceptualization, Methodology, Investigation, Visualization, Resources, Writing-review.

Data availability

Data will be available on the request.

Conflicts of interest

The authors declare that they have no known competing financial interests or personal relationships that could have appeared to influence the work reported in this paper.

Supplementary information

No additional information was provided by the authors.

Ethical approval

Not applicable.

References

1. Lunetto V, De Maddis M, Lombardi F, Russo Spena P (2025) A Review of Friction Stir Welding of Industrial Alloys: Tool Design and Process Parameters. J. Manuf. Mater. Process. 9: 36. doi: 10.3390/jmmp9020036

2. Shashi Kumar S, Murugan N, Ramachandran KK (2018) Microstructure and mechanical properties of friction stir welded AISI 316L austenitic stainless steel joints. J. Mater. Process. Technol. 254:79-90. doi:10.1016/j.jmatprotec.2017.11.015

3. Shashi Kumar S, Murugan N (2021) An Insight to Friction Stir Welding of AISI 316L Stainless Steel. Scholar's Press. OmniScriptum S.R.L.Chisinau, Republic of Moldova, 2021.

4. Spigarelli S (2022). A unified constitutive approach for creep response of AISI 316 steel produced by conventional technologies or additive manufacturing techniques, Materials at High Temperatures 40:48-62. doi:10.1080/09603409.2022.2146309

5. Lu J, Hultman L, Holmström E, Antonsson KH, Grehk M, Li W, Vitos L, Golpayegani A (2016). Stacking fault energies in austenitic stainless steels. Acta Mater. 111:39-46. doi:10.1016/j.actamat.2016.03.042

6. Kestenbach HJ, Luiz Da Silveira T, Monteiro SN (1976). On subgrain formation during creep of 316 stainless steel. Metallurgical Transaction A 7:155–158. doi:10.1007/BF02644054

7. Kestenbach HJ, Krause W, da Silveira TL (1978) Creep of 316 stainless steel under high stresses. Acta Metall. 26:661-670. doi:10.1016/0001-6160(78)90016-0

8. Mathew MD, Sundararaman M, Mannan SL (1997) Dislocation substructure and precipitation in type 316 stainless steel deformed in creep. Mater. Trans. 38:37-42. doi:10.2320/matertrans1989.38.37

9. Harvey PD (1982). Engineering Properties of Steel, ASM; Metals Park, Ohio, pp.296-297.

10. Choudhary BK (2014) Influence of strain rate and temperature on tensile deformation and fracture behavior of type 316L(N) austenitic stainless steel. Metall. Mater. Trans. A, 45A:302–316.doi:10.1007/s11661-013-1978-2

11. Morris DG, Harries DR (1978). Creep and rupture in Type 316 stainless steel at temperatures between 525 and 900°C. Part I: creep rate. Metal science 12:525-531. doi:10.1179/msc.1978.12.11.525

12. Rieth M, Falkenstein A, Graf P, Heger S, Jaentsch U, Klimiankou M, Materna-Morris E, Zimmermann H (2004).Creep of the austenitic steel AISI 316L(N). Experiments and models. Research Center Karlsruhe GmbH Technology and Environment (Germany). Institute for Materials Research - Nuclear Fusion program, Report FZKA-7065, November 2004.

https://d-nb.info/973572558/34

13. Mathew MD, Laha K, Ganesan V (2012). Improving creep strength of 316L stainless steel by alloying with nitrogen. Mater. Sci. Eng. A535:76-83. doi:10.1016/j.msea.2011.12.044

14. Sandström S, Andersson HCM (2008). Creep in phosphorus alloyed copper during power-law breakdown. Journal of Nuclear Materials 372:76-88. doi:10.1016/j.jnucmat.2007.02.005

15. Sandström S (2012). Basic model for primary and secondary creep in copper. Acta Mater. 60:314-322. doi:10.1016/j.actamat.2011.09.052

16. Sandström R (2016). Influence of phosphorus on the tensile stress strain curves in copper. J. Nucl. Mater. 470:290-296. doi:10.1016/j.jnucmat.2015.12.024

17. Sandström S (2017). The role of cell structure during creep of cold worked copper. Mater. Sci. Eng. A674:318-327. doi:10.1016/j.msea.2016.08.004

18. Korzhavyi PA, Sandström R (2015). First-principles evaluation of the effect of alloying elements on the lattice parameter of a 23Cr25NiWCuCo austenitic stainless steel to model solid solution hardening contribution to the creep strength (2014). Mater. Sci. Eng. A626:213–219. doi:10.1016/j.msea.2014.12.057

19. Sandström (2022). Formation of Cells and Subgrains and Its Influence on Properties. Metals, 12: 497. doi:10.3390/met12030497

20. He J, Sandström R (2017). Basic modelling of creep rupture in austenitic stainless steels. Theor. Appl. Fract. Mech. 89:139–146. doi:10.1016/j.tafmec.2017.02.004

21. Sandström R (2024). Basic Modeling and Theory of Creep of Metallic Materials, Springer Series in Materials Science 339:145-168. doi:10.1007/978-3-031-49507-6_8

22. Kassner ME,Perez-Prado MT (2001). Five-power-law creep in single phase metals and alloys. Prog. Mater. Sci. 45:1-102. doi:10.1016/S0079-6425(99)00006-7

23. Tamura M (2018) Relation between sub-grain size and dislocation density during steady-state dislocation creep of polycrystalline cubic metals. J. Mater. Sci. Res. 7:26-45. doi:10.5539/jmsr.v7n4p26

24. Sandström R, Zhang J (2021). Modeling the Creep of Nickel. J. Eng. Mater. Technol. 143: 041011:1-041011:5. doi:10.1115/1.4051421

25. Cuddy LJ (1970) Internal stresses and structures developed during creep. Metall. Trans. 1:395–401. doi:10.1007/BF02811548

26. Michel DJ, Moteff J, Lovell AJ (1973) Substructure of type 316 stainless steel deformed in slow tension at temperatures between 21° and 816°C. Acta Metall. 21:1269-1277. doi:10.1016/0001-6160(73)90168-5

27. Kassner ME, Elmer JW, Echer CJ (1986) Changes in the subboundary mesh size with creep strain in 304 stainless steel. Metall. Trans. 17:2093-2097. doi:10.1007/BF02645011

28. Peng K, Qian K, Chen W (2004). Effect of dynamic strain aging on high temperature properties of austenitic stainless steel. Mater. Sci. Eng. A379:372–377. doi:10.1016/j.msea.2004.03.004

29. Raj SV, Iskovitz IS, Freed AD (1996). Modeling the role of dislocation substructure during class m and exponential creep, in Krausz AS, Krausz K (Editors) Unified Constitutive Laws of Plastic Deformation, Academic Press, San Diego, pp. 343-439.

30. Monteiro SN, Cassiano Nascimento LF, Simonassi NT, Lima ES, Santos de Paula A, de Oliveira Braga F (2018) High temperature work hardening stages, dynamic strain aging and related dislocation structure in tensile deformed AISI 301 stainless steel. J. Mater. Res. Technol. 7:571-577. doi:10.1016/j.jmrt.2018.06.020

31. Sikka VK, Nahm H, Moteff J (1975) Some Aspects of Sub-boundary and Mobile Dislocations during High Temperature Creep of AISI 316 and 304 Stainless Steels. Mater. Sci. Eng. 20:55-62. doi:10.1016/0025-5416(75)90130-5

32. Kocks UF, Mecking H (2003). Physics and phenomenology of strain hardening: the FCC case. Prog. Mater. Sci. 48:171–273. doi:10.1016/S0079-6425(02)00003-8

33. Orlová A (2001) Subgrain size in view of the composite model of dislocation structure. Mater. Sci. Eng. A297:281-285. doi:10.1016/S0921-5093(00)01697-X

34. Brown DW, Adams DP, Balogh L, Carpenter JS, Clausen B, King G, Reedlunn B, Palmer TA, Maguire MC, Vogel SC (2017) In situ neutron diffraction study of the influence of microstructure on the mechanical response of additively manufactured 304l stainless steel. Metall. Mater. Trans. 48A: 6055-6069. doi:10.1007/s11661-017-4330-4

35. Koneva NA, Starenchenko VA, Lychagin DV, Trishkina LI, Popova NA, Kozlov EV (2008). Formation of dislocation cell substructure in face-centred cubic metallic solid solutions. Mater. Sci. Eng. A483–484:179–183. doi:10.1016/j.msea.2006.08.140

36. Ganesan V, Mathhew MD, Parameswaran P, Laha K (2013) Effect of nitrogen on evolution of dislocation substructure in 316ln ss during creep. Procedia Engineering 55:36-40. doi:10.1016/j.proeng.2013.03.215

37. Yurechko M, Skrypnik A, Wedemeyer O, Konys J, Schroer C (2022) Creep of 316L austenitic steel at 450–550 °C in static lead-bismuth eutectic covered by argon-hydrogen gas. J. Nucl. Mater. 558:153344. doi:10.1016/j.jnucmat.2021.153344

38. Calmunger M, Chai G, Eriksson R, Johansson S, Moverare JJ (2017) Characterization of austenitic stainless steels deformed at elevated temperature. Metall. Mater. Trans. A48:4525-4538. doi:10.1007/s11661-017-4212-9

39. Brinkman CR (2001) Elevated-Temperature Mechanical Properties of an Advanced-Type316 Stainless Steel. J. Press. Vessel Technol. 123:75-80. doi:10.1115/1.1343911

40. Staker MR, Holt DL (1972) The dislocation cell size and dislocation density in copper deformed at temperatures between 25 and 700°C. Acta Metall. 20:569-579. doi:10.1016/0001-6160(72)90012-0

41. Keh AS, Weissmann S (1963) in Thomas G, Washburn J (Editors) Electron Microscopy and Strength of Crystals, Interscience Publisher, p. 231.

42. Griffiths D, Riley JN (1966) Dislocation arrangements in deformed polycrystalline 3% silicon-iron. Acta Metall. 14:755-773. doi:10.1016/0001-6160(66)90123-4

43. Langford G, Cohen M (1969) Strain hardening of iron by severe plastic deformation. Transaction American Society of Metals 62:623.

44. Kuhlmann-Wilsdorf D (1970) A critical test on theories of work-hardening for the case of drawn iron wire. Metall. Trans.1:3173–3179. doi:10.1007/BF03038434

45. Challenger KD, Moteff J (1973) Quantitative characterization of the substructure of AISI 316 stainless steel resulting from creep. Metall. Trans. 4:749–755. doi:10.1007/BF02643084

46. Holt DL (1970) Dislocation Cell Formation in Metals. J. Appl. Phys. 41:3197–3201. doi:10.1063/1.1659399

47. Monteiro SN, Santos da Luz F, Pinheiro WA, Mendonça Brandão LP, de Oliveira Braga F, Salgado de Assis F (2017) Creep parameters and dislocation substructure in aisi 316 austenitic stainless steel from 600ºC to 800ºC. Mater. Res. 20:231-235. doi:10.1590/1980-5373-MR-2016-0998

48. Spigarelli S, Sandström R (2018) Basic creep modelling of aluminium. Mater. Sci. Eng. A711:343-349. doi:10.1016/j.msea.2017.11.053

49. Spigarelli S, Paoletti C (2018) A unified physical model for creep and hot working of Al-Mg solid solution alloys. Metals 8:9. doi:10.3390/met8010009

50. Kassner ME (2004) Taylor hardening in five-power-law creep of metals and Class M alloys. Acta Mater. 52:1–9. doi:10.1016/j.actamat.2003.08.019

51. Kassner ME (1994) The Effect of Low-Angle and High-Angle Grain Boundaries on Elevated Temperature Strength. RS Online Proceedings Library 362:157–162. doi:10.1557/PROC-362-157

52. Kassner ME, Miller AK, Sherby OD (1982) The separate roles of subgrains and forest dislocations in the isotropic hardening of type 304 stainless steel. Metall. Trans. A13: 1977–1986. doi:10.1007/BF02645943

53. Francke D, Pantleon W, Klimanek P (1996) Modelling the occurrence of disorientations in dislocation structures. Comput. Mater. Sci. 5:111-125. doi:10.1016/0927-0256(95)00062-3

54. Wang J, Zhang X (2016) Twinning effects on strength and plasticity of metallic materials. MRS Bulletin, 41:274-281. doi:10.1557/mrs.2016.67

55. Bufford D, Wang H, Zhang X (2013) Thermal stability of twins and strengthening mechanisms in differently oriented epitaxial nanotwinned Ag films. J. Mater. Res. 28:1729 – 1739. doi:10.1557/jmr.2013.50

56. Li X, Wei Y, Lu L, Lu K, Gao H (2010) Dislocation nucleation governed softening and maximum strength in nano-twinned metals. Nature 464:877-880. doi:10.1038/nature08929